THE JOURNAL OF PHYSICAL CHEMISTRY C
Article
pubs.acs.org/JPCC

Ab Initio Thermodynamics and Kinetics for Coalescence of Two-Dimensional Nanoislands and Nanopits on Metal (100) Surfaces

Yong Han,*[,†] Conrad R. Stoldt,[‡,∥] Patricia A. Thiel,[‡,§] and James W. Evans*[,†,§]

[†]Department of Physics and Astronomy, [‡]Department of Chemistry, and [§]Ames Laboratory − U.S. Department of Energy, Iowa State University, Ames, Iowa 50011, United States

Supporting Information

ABSTRACT: Postdeposition coalescence or sintering of pairs of low-strain two-dimensional nanoislands and nanopits on unreconstructed metal (100) surfaces is typically mediated by diffusion along step edges, and is highly sensitive to the associated kinetics. Thus, for selected systems, we provide an ab initio density functional theory (DFT) level description of both system thermodynamics and kinetics. Specifically, we assess lateral pair and trio interactions both conventionally with adatoms at 4-fold hollow adsorption sites, and unconventionally with one adatom at the bridge-site transition state for hopping. Rather than use standard cluster expansion algorithms, these interactions are determined subject to the constraint that key step-edge properties are recovered exactly. Together, both classes of interactions determine barriers for edge diffusion processes for any local step configuration, including diffusion along close-packed ⟨110⟩ edges, kink rounding, meandering processes at kinked ⟨100⟩ steps, and extraction processes at pit corners. Our formalism applies for homoepitaxial systems, and also for several lattice-matched heteroepitaxial systems. The barriers provide input for stochastic models of nanocluster evolution, which are analyzed by kinetic Monte Carlo simulation. Such modeling with DFT energetics from the PBEsol functional recovers extensive experimental observations of both the time scale and the island-size dependence for sintering of Ag islands on Ag(100). Description of pit sintering on Ag(100) is more delicate, being sensitive to specific unconventional trio interactions.

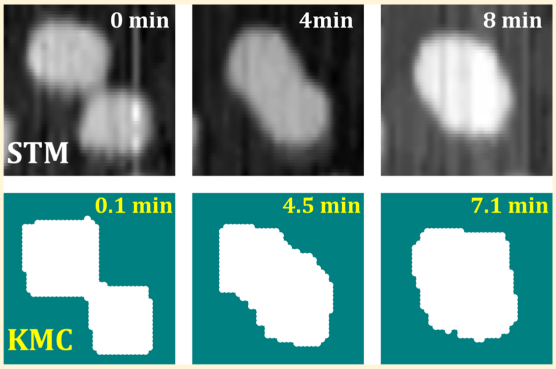

1. INTRODUCTION

Coalescence or sintering of pairs of epitaxial or crystalline nanoclusters (NCs) is a key pathway for destabilization of functional nanostructured systems. NC diffusion and coalescence provides a so-called Smoluchowski ripening pathway for coarsening of ensembles of such NCs.[1] This issue is relevant not just for two-dimensional (2D) or three-dimensional (3D) surface-supported NCs,[1−6] but also for solution-phase 3D NCs.[7−10] A typical scenario is that a dumbbell-shaped NC formed by impingement of two convex NCs evolves to a larger convex NC ultimately with an equilibrium Wulff shape; see Figure 1. This behavior can be assessed experimentally by scanning tunneling microscopy (STM) for 2D and 3D NCs on surfaces,[1−4] and by transmission electron microscopy (TEM) for 3D NCs in solution.[7,9,10] Evolution is often mediated by periphery diffusion (PD), that is, edge diffusion for 2D NCs, and surface diffusion for 3D NCs. Analogous coalescence or sintering behavior might also be considered for pairs of pits on 2D surfaces, or for pairs of 3D voids within crystalline solids, although the latter is not readily imaged. Pits or voids might be described as vacancy NCs. Given the epitaxial or crystalline structure of the system for either atomic or vacancy NCs, stochastic lattice-gas modeling is naturally suited to track such evolution where prescription of PD rates consistent with detailed balance for a suitable description of system energetics will ensure evolution to the appropriate Wulff shape.[2,8,11,12]

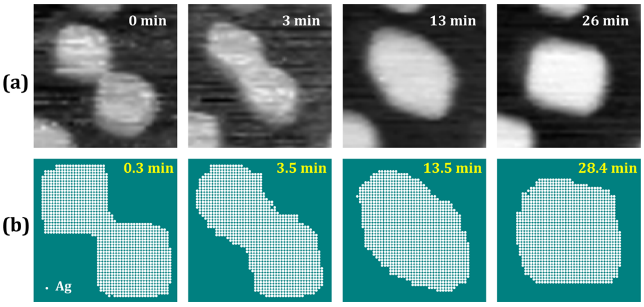

Figure 1. Illustrative images of corner-to-corner sintering of a 7.3 × 7.0 nm^2 + 7.9 × 7.6 nm^2 pair of Ag adatom NCs on Ag(100) at 295 K: (a) STM observations of shape evolution; and (b) corresponding KMC simulation from our model described in sections 3 and 4. Island sizes in the KMC simulations are chosen to match experimental size from the STM images. Overall image sizes differ.

Received: July 22, 2016
Revised: September 1, 2016
Published: September 2, 2016

DOI: 10.1021/acs.jpcc.6b07328
J. Phys. Chem. C 2016, 120, 21617−21630

Such model behavior is precisely assessed by kinetic Monte Carlo (KMC) simulation.[2,4,5,8]

Some stochastic lattice-gas modeling studies, particularly for sintering of 3D NCs,[11,12] have tended to use generic prescriptions of PD kinetics. However, previous analyses for 2D surface systems have indicated that behavior at the nanoscale is exquisitely sensitive to system-specific details, for example, reduced rates for transport around kinks or corners versus along close-packed steps.[2,4,13] These details, and also the possible presence on the nanoscale of perfectly straight "faceted" close-packed step edges, which are free of kinks, can also produce scaling behavior with NC size fundamentally different from that of generic prescriptions of kinetics or from coarse-grained mesoscopic treatments.[13−16] Behavior for 3D NCs will by analogy be sensitive to the presence of faceted NC shapes, and to differences between rates of diffusion across versus between facets.[17]

Our focus here is on 2D NCs on crystalline surfaces, which are usually described as islands or pits. Thus, we will exclusively use this terminology below. Specifically, we consider PD-mediated coalescence and reshaping of both epitaxial 2D (single-atom-high) nanoislands and 2D (single-atom-deep) nanopits on unreconstructed metal (100) surfaces. See again Figure 1. We restrict our consideration to homoepitaxial and low-strain heteroepitaxial systems where PD involves adatom hopping rather than exchange with the substrate. We note that treatment of both thermodynamics and kinetics is significantly more challenging if strain effects are important. Our study will provide a tailored formalism utilizing density functional theory (DFT) to determine not just ab initio thermodynamics, but also ab initio periphery diffusion barriers for all possible local periphery configurations. Extensive DFT analysis will be performed utilizing the plane-wave VASP code[18] using slab geometries. Care must be taken to ensure reliable results from such analysis, for example, avoiding quantum size effects (QSEs) particularly for Ag and Cu slabs.[19,20] For this reason, we utilize a slab with a thickness of 15 monatomic layers (referred to below as monolayers or MLs) to represent the substrate in contrast to the common choice of 5−6 MLs. We describe the otherwise standard procedures for our DFT analysis in the Supporting Information. Results from DFT analysis presented in the main text will be based on the Perdew−Burke−Ernzerhof (PBE) generalized-gradient-approximation (GGA) functional for solids.[21] The abbreviation "PBEsol" is used to denote this functional. Corresponding results from the PBE GGA functional,[22] which are not used in this study, are also given in the Supporting Information. This DFT energetics provides input to stochastic lattice-gas modeling, which is analyzed by KMC simulation. The KMC simulation results will be compared against experimental STM results for the Ag/Ag(100) system.

While this contribution focuses on model development, we briefly describe the procedure for obtaining the STM data against which the model is compared. We used an Omicron STM housed in an ultrahigh vacuum chamber with a base pressure of below 10^{-10} Torr. Initial film configurations were created by evaporative deposition of Ag onto a Ag(100) single crystal. Large-area scans of postdeposition evolution were taken at intervals of 3−15 min. For deposition of low submonolayer coverages, various examples of island diffusion and collision with other islands were observed. Pit configurations were produced by near-monolayer depositions. The images are typically obtained in the constant-current mode, with 1.0−1.1 V bias voltage and 3.0−3.4 nA tunneling current. STM tip effects do not significantly influence nanostructure evolution. Island dimensions are estimated from the scan profiles typically taking the region that is higher than the full width at half-maximum (fwhm). This procedure may be naturally refined to account for artificially increased size due to any double-tip effects; for example, see the first frame in Figure 1a. For more details, see refs 1, 2, and 4.

As an aside, in addition to considering coalescence of NC pairs, our formalism also describes and elucidates NC diffusion, which enables the coalescence of initially separated clusters. Furthermore, this formalism enables description of the evolution of more complicated irregular NC shapes, for example, those formed by coalescence of multiple islands, or those obtained for pits by deposition of high submonolayer coverages leading to a near-complete first adlayer.[23]

Stochastic lattice-gas modeling of these processes must reliably input lateral interactions between adatoms at 4-fold-hollow (4fh) adsorption sites on the metal (100) surface, as they determine adlayer thermodynamics. We will describe these as conventional lateral interactions, as they have been considered in numerous studies of adlayer thermodynamics over the last few decades,[24,25] and we shall refer to them as ω-interactions. Precise description must incorporate not just the dominant nearest-neighbor (NN) attractive interactions, but generally also longer-range pair interactions and many-body interactions. We mention three strategies for the determination of ω-interactions:

(i) True interaction values can be determined from a sequence of large-unit-cell DFT calculations involving an isolated adatom, adatom pair, adatom triple, etc., at 4fh sites. Using a many-body expansion, pair interactions come from subtracting adatom adsorption energies from the total adsorption energy for a pair; trio interactions come from subtracting pair interactions and adsorption energies from total trio energies; etc.

(ii) A standard cluster expansion (CE) approach determines values for a selected subset of pair, trio, etc., interactions to consistently recover energies of a subset of periodic adlayer configurations, typically with smaller unit cells. The determined interaction values are effective because they incorporate the effect of neglected interactions. Various strategies for optimal implementation have been developed and applied specifically to surface systems.[24,25] While the approach is formally validated when retaining a complete set of interactions,[26] a key practical requirement (and possible limitation) is robustness when retaining smaller sets of interactions.

(iii) An alternative modified approach pursued here is to select interactions in a way tuned to the application of interest. In this case, we require that selected interactions recover some aspects of step-edge thermodynamics. Specifically, we focus on energetics related to step stiffness, as this property directly impacts step-edge evolution.

Note that lateral adatom relaxation impacts the values of the above pair, trio, etc., interactions. Furthermore, relaxation for isolated adatom pairs, triples, etc., in periodic adlayers will differ from that at step edges.[24,27] Thus, implementation of the various approaches described above produces somewhat differing ω-values, a feature we illustrate in the following sections and the Supporting Information.

Our central goal is to model PD-mediated NC evolution in metal (100) systems with an ab initio treatment of PD kinetics. Adatom hop rates for all local environments are assumed to have the Arrhenius form $h = \nu\, \mathrm{e}^{-E_{\mathrm{act}}/(k_{\mathrm{B}}T)}$, where k_{B} is Boltzmann's constant, and T is the surface temperature. We adopt a common prefactor with a typical value of $\nu \approx 3.33 \times 10^{12}$/s. The activation barriers, E_{act}, for terrace diffusion, various local step-edge configurations, etc., are given by the general relation:

$$E_{\mathrm{act}} = E_{\mathrm{d}} + \Phi_{\mathrm{TS}} - \Phi_{\mathrm{init}} \tag{1}$$

where E_{d} is the terrace-diffusion barrier for isolated adatoms; Φ_{TS} and Φ_{init} denote the total lateral interaction energies at the transition state (TS) and the initial state before hopping, respectively. Φ_{init} is determined by summing over relevant ω's involving the hopping adatom in the initial state. Note that the total interaction, Φ_{fnl}, in the final state after hopping can be determined by summing over the relevant ω's. A common bond-breaking or initial-value approximation sets $\Phi_{\mathrm{TS}} = 0$.[28] A more general approach in the spirit of Brønsted−Evans−Polanyi or Butler−Volmer relations writes $\Phi_{\mathrm{TS}} = c_1\Phi_{\mathrm{init}} + c_2\Phi_{\mathrm{fnl}}$, where for diffusion processes one sets $c_1 = c_2$, and the most common choice is $c_1 = 1/2$.[29−31] However, either of these approaches gives a poor description of PD kinetics for metal (100) systems.[28]

Instead, we emphasize the long-recognized feature[32] that Φ_{TS} is determined by a distinct set of lateral interactions, which specifically describe the interaction of one adatom at a TS for hopping with other nearby adatoms, all of which are at 4fh sites.[33−38] These interactions are distinct from and independent of the ω-interactions determining Φ_{init} and Φ_{fnl}. Furthermore, because they have received relatively little attention, we describe them as unconventional lateral interactions, and we shall refer to them as ϕ-interactions. Analysis of diffusion on metal (100) surfaces based on semiempirical potentials found some success with a simple choice for the dominant pair ϕ-interaction at the TS.[33] Another study used DFT to directly assess selected pair ϕ-interactions for certain Al diffusion processes on Al(110) in the presence of a single nearby atom.[34] Our approach is to systematically determine a complete set of unconventional pair, trio, etc., ϕ-interactions with one adatom at the bridge-site TS for hopping and one or more other adatoms at nearby stable adsorption sites. We can then precisely obtain Φ_{TS} by summing over appropriate ϕ's with the assumption that the bridge-site TS location is not significantly impacted by the local environment. Thus, utilizing E_{d} as well as both ω's and ϕ's, we reliably reconstruct E_{act} for general step-edge configurations.[35−38] In determining an appropriate set of ϕ's, our guiding philosophy will be to recover key edge-diffusion barriers of relevance to our application. Access to general E_{act} allows KMC simulation of NC sintering with ab initio kinetics.[35−38]

In section 2, we provide some background on step-edge properties for metal (100) surfaces. In section 3, we implement strategies to determination of conventional ω-interactions. In section 4, we determine unconventional ϕ-interactions. Sections 2, 3, and 4 focus on and report DFT results for key quantities for Ag(100) and Cu(100), noting extensive experimental analysis of coalescence and reshaping for Ag,[2,4,39] and limited observations for Cu.[40] Section 5 discusses other homoepitaxial systems, specifically Pd, Ni, Rh, Fe, Nb, and Ta. It also briefly describes low-strain heteroepitaxial metal (100) systems including Au/Ag(100), Pt/Pd(100), Ir/Rh(100), and Nb/Ta(100). In some cases, our formalism applies, but we find that it is inapplicable in others due to strong intermixing. KMC analysis of our stochastic model with ab initio kinetics for coalescence and reshaping of Ag NCs and pits on Ag(100) is provided in section 6, where we successfully compare predictions with extensive experimental data. Further discussion and conclusions are provided in section 7.

2. STEP-EDGE THERMODYNAMICS, DIFFUSION, AND EVOLUTION

2.1. Step-Edge Thermodynamics.

Step energy, β, measures the energy cost per unit length to form a step. The dependence on step orientation controls the equilibrium island and pit shape, as quantified by a Wulff construction.[41] We will write, for example, $\beta_{\langle 100\rangle}$, to denote the β value for a special orientation $\langle 100\rangle$, etc., and $\beta(\theta)$, to denote the general dependence on step orientation described by the angle θ relative to the close-packed direction. In a simplified picture for fcc metal (100) surfaces, islands or pits are dominated by close-packed $\langle 110\rangle$ and diagonal kinked $\langle 100\rangle$ step edges, and their octagonal equilibrium shape is determined by the ratio $\beta_{\langle 100\rangle}/\beta_{\langle 110\rangle}$.[42] In a classic Ising lattice-gas model with just NN interactions ω_{NN} (which also corresponds to an NN bond dissociation energy), one has that $a\beta_{\langle 110\rangle} = -\omega_{\mathrm{NN}}/2$ and $\beta_{\langle 100\rangle}/\beta_{\langle 110\rangle} = \sqrt{2}$ at $T = 0$ K, where a is the surface lattice constant. A standard procedure for theoretical determination of $\beta_{\langle 110\rangle}$ and $\beta_{\langle 100\rangle}$ is as follows:[41] first determine the bulk energy per atom, $\varepsilon_{\mathrm{bulk}}$; then determine the total energy of a perfect slab with (100) faces, and use $\varepsilon_{\mathrm{bulk}}$ to extract the surface energy, $\gamma_{(100)}$, for the (100) plane; finally, determine the total energy for a slab with periodically alternating ascending-and-descending steps of a specified orientation, and then extract the associated step energy using $\varepsilon_{\mathrm{bulk}}$ and $\gamma_{(100)}$. However, any errors in $\varepsilon_{\mathrm{bulk}}$ and $\gamma_{(100)}$ produce significant errors in estimates of β's. For this reason, we adopt a different strategy described in section S3.

Next, we describe other quantities, which are particularly relevant for our analysis of step-edge evolution. The first thermodynamic quantity is step stiffness, $\beta^*(\theta) = \beta(\theta) + \mathrm{d}^2\beta(\theta)/\mathrm{d}\theta^2$, which controls both equilibrium step fluctuations and also nonequilibrium evolution.[41] As a convenient way to assess step stiffness, at least for lower T, it is instructive to consider step excitation energies, ΔE. We define $\Delta E_{\langle 110\rangle}$ as the cost to displace an edge atom from an otherwise perfectly straight $\langle 110\rangle$ step and place it adjacent to the step, thereby creating a separated atom indentation−protrusion pair; see Figure 2a. $\Delta E_{\langle 100\rangle}$ is defined analogously; see Figure 2b. For a $\langle 110\rangle$ step, such an excitation creates four kinks, and it is natural to define an associated kink creation energy as $\varepsilon_{\mathrm{k}} = \Delta E_{\langle 110\rangle}/4$.[43,44] Furthermore, it follows that $\beta^*_{\langle 110\rangle} \propto \mathrm{e}^{\varepsilon_{\mathrm{k}}/(k_{\mathrm{B}}T)}$ for low T.[41] In the Ising lattice-gas model, one has that $\Delta E_{\langle 110\rangle} = -2\omega_{\mathrm{NN}}$ and then $\varepsilon_{\mathrm{k}} = -\omega_{\mathrm{NN}}/2$. For the kinked $\langle 100\rangle$ step, one expects a lower $\Delta E_{\langle 100\rangle}$, and thus that $\beta^*_{\langle 100\rangle}$ is lower than $\beta^*_{\langle 110\rangle}$. Indeed, $\Delta E_{\langle 100\rangle} = 0$ in the Ising model, although $\Delta E_{\langle 100\rangle} > 0$ in real systems.

Another thermodynamic quantity critical for analysis of step-edge evolution is the formation energy for creation of an edge atom by extracting the atom from a kink site to a straight $\langle 110\rangle$ step edge;[41] see Figure 2c. This quantity is denoted by $E_{\mathrm{e}}^{\mathrm{form}}$, which for the Ising model is given by $E_{\mathrm{e}}^{\mathrm{form}} = -\omega_{\mathrm{NN}}$. As extraction of an atom from a kink site creates two additional kinks, one might expect that $\varepsilon_{\mathrm{k}} \approx -E_{\mathrm{e}}^{\mathrm{form}}/2$ and thus that $E_{\mathrm{e}}^{\mathrm{form}} \approx \Delta E_{\langle 110\rangle}/2$ apply for systems with more general interactions than the Ising model.

We obtain precise estimates of $E_{\mathrm{e}}^{\mathrm{form}}$, $\Delta E_{\langle 110\rangle}$, and $\Delta E_{\langle 100\rangle}$ from DFT analysis using the 5×4, 4×5, and $3\sqrt{2} \times 3\sqrt{2}$ unit cell configurations, respectively, shown in Figure 2a−c.

DOI: 10.1021/acs.jpcc.6b07328
J. Phys. Chem. C 2016, 120, 21617−21630

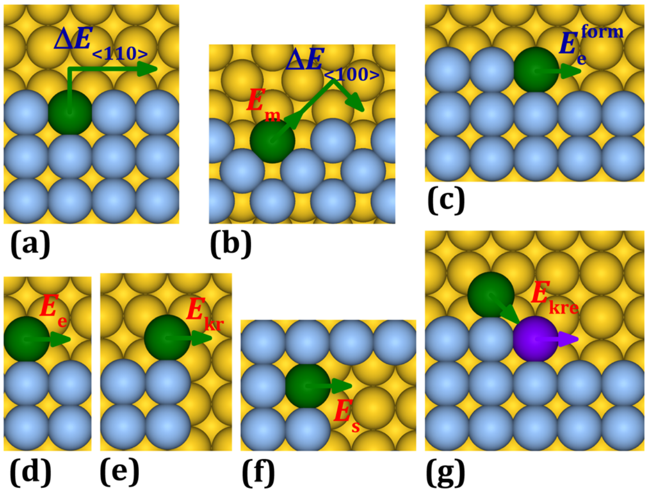

Figure 2. Schematics for (a) ⟨110⟩ step excitation; (b) ⟨100⟩ step excitation; (c) edge atom formation by extraction from a kink; (d) edge diffusion; (e) corner rounding; (f) atom sliding from a pit corner; and (g) two-atom near-kink exchange. Indicated image sizes are the unit cells used for our DFT analysis.

Results for Ag and Cu using the PBEsol functional are shown in Table 1. Note that the relation $E_e^{\text{form}} \approx \Delta E_{110}/2$ suggested above is well-satisfied. Also, the experimental estimate of $\varepsilon_k = \Delta E_{\langle 110\rangle}/4 = 0.128$ eV for Cu(100)[41] is close to but somewhat below our PBEsol value of 0.148 eV.

Table 1. PBEsol Estimates of the Edge-Atom Formation Energy E_e^{form} and Excitation Energies ΔE (in eV) for Straight Steps of Ag(100) and Cu(100)

	E_e^{form}	$\Delta E_{\langle 110\rangle}$	$\Delta E_{\langle 110\rangle}$
Ag	0.239	0.482	0.021
Cu	0.303	0.592	0.048

2.2. PD Kinetics.

Particularly relevant for this study is an atomistic-level description of step-edge diffusion, that is, PD, and its connection to PD-mediated sintering of NCs. Our results for key barriers for Ag(100) and Cu(100) systems using the PBEsol functional are presented in Table 2. One naturally considers edge diffusion along straight close-packed ⟨110⟩ steps with a barrier E_e (Figure 2d), which is expected to be well below the terrace-diffusion barrier E_d. In addition, for metal (100) surfaces, one anticipates an additional barrier, δ_{kr}, for edge atoms to round kinks or corners (Figure 2e), usually referred to as the kink Ehrlich–Schwoebel barrier. Thus, the total kink or corner rounding barrier is $E_{kr} = E_e + \delta_{kr}$. The kinetics of meandering of diagonal ⟨100⟩ step edges between configurations with similar energies is controlled by the barrier E_m for the process indicated in Figure 2b. We have performed extensive DFT analysis to directly determine E_e, E_{kr}, and E_m, as well as E_d. For terrace diffusion, the dominant pathway is well-accepted to be hopping rather than exchange-mediated processes[45] on Ag(100) and Cu(100) surfaces. Thus, for E_d, we use a 4 × 4 unit cell determining the difference in adsorption energy at the bridge site TS for hopping and the initial 4fh site. For E_e, we use a 2 × 4 unit cell comparing energy at a 4fh site and the bridge TS site at a close-packed ⟨110⟩ step edge as indicated in Figure 2d. For E_{kr}, we use a 3 × 4 unit cell comparing 4fh and TS energies also indicated in Figure 2e. We also used a 4 × 4 unit cell to check the result, and found that there is a tiny change of ~8 meV in E_{kr}. For E_m, we use the $3\sqrt{2} \times 3\sqrt{2}$ unit cell shown in Figure 2b. In addition, we have determined the barrier, E_s, for a process involving sliding of an adatom out of the corner of a square pit using a 3 × 5 unit cell shown in Figure 2f. We anticipate that this process will be important for sintering and diffusion of pits.[46] We also determine the barrier, E_b, for extraction from a close-packed ⟨110⟩ step edge. All above barriers have been estimated using PBEsol functional and are shown in Table 2.

Table 2. PBEsol Estimates of Activation Barriers (in eV) for Key Step-Edge Diffusion Processes for Ag(100) and Cu(100)[a]

	E_e	E_{kr}	E_m	E_s	E_b
Ag	0.291	0.524	0.601	0.587	0.835
Cu	0.334	0.624	0.705	0.681	0.984

[a] We also obtain E_d = 0.538 (0.616) eV for Ag (Cu).

For substantial reshaping and long-range cluster diffusion mediated by edge diffusion, atoms must be extracted from kinks and diffuse not just along straight ⟨110⟩ steps, but also around kinks and corners. Thus, the effective or overall barrier for this process is expected to be given by $E_{\text{eff}} = E_e^{\text{form}} + E_e + \delta_{kr} = E_e^{\text{form}} + E_{kr}$.[4,13,23] From the above results, we extract PBEsol values of E_{eff} = 0.763 eV for Ag, and E_{eff} = 0.927 eV for Cu. These barriers will control the time scale for reshaping.

As an aside, kink or corner rounding in the above analysis was assumed to occur via hopping. In this case, the barrier should be effectively the same for single-atom-high kinks or multiatom-high kinks where the latter are reasonably described as corners. The reason is that in both cases, the TS occurs early in the corner rounding process where interactions with the hopping atom are effectively the same for kink and corner configurations. Rounding of single-atom-high kinks via exchange where the diffusing atom pushes the kink atom along the step (see Figure 2g) could potentially be energetically more favorable than the hopping pathway. Exchange seems unlikely for corner rounding where the original corner atom is pushed out to a low-coordinated site rather than along a step edge. We have performed the climbing nudged elastic band (cNEB) calculations[47] using a 5 × 5 unit cell but a thinner slab (to reduce computational expense) to assess the barrier for this exchange process. This analysis indicates that the barrier is around 0.1 eV higher than for hopping for Cu, so this process is not significant. For details, see the Supporting Information.

2.3. Coarse-Grained Step-Edge Evolution.

In a coarse-grained description of PD-mediated step-edge evolution,[23,41] the normal step velocity is given by $v_n \propto -\nabla_s J_{PD}$ as the gradient along the step of the edge diffusion flux J_{PD}. Here, s measures arc length. In addition, one has that $J_{PD} \propto -\sigma_{PD}(\theta)\nabla_s\mu$, where σ_{PD} is an associated orientation-dependent step mobility, and μ denotes the step chemical potential. Finally, one has that $\mu \propto \beta^*(\theta)\nabla\kappa$, where κ is the step curvature. This deterministic formulation can effectively describe the reshaping of larger structures.[22] For description of cluster diffusion, one should add suitable noise terms to generate an appropriate Langevin evolution equation.[48] Ignoring any θ-dependence, the product $\sigma_{PD}\beta^*$ controls the time scale for these processes. Rigorous analysis of σ_{PD} is difficult, but it can be shown that its effective barrier matches E_{eff}, at least for a simple model with $E_{kr} = 0$.[49]

Finally, we should also emphasize that it is now well-recognized that coarse-grained continuum formulations of

DOI: 10.1021/acs.jpcc.6b07328
J. Phys. Chem. C 2016, 120, 21617–21630

cluster reshaping can fail to capture distinct behavior on sufficiently small nanoscales. Distinct scaling with relevant linear size, L, of relaxation times or cluster diffusion rates occurs when L drops below some relevant characteristic length, L_c. This L_c is determined by system energetics, and may correspond to, for example, the mean separation of kinks along ⟨110⟩ step edges, $L_k \approx a\,e^{\varepsilon_k/(k_BT)/2}$, or the kink Ehrlich–Schwoebel length, $L_{kr} \approx a\,e^{\delta_{kr}/(k_BT)}$.[1,2,13–16]

3. CONVENTIONAL LATERAL ADATOM ω-INTERACTIONS

3.1. ω-Interactions and Key Thermodynamic Quantities. First, we discuss the selection and determination of conventional ω-interactions, as illustrated in the top panel of Figure 3. We will label pair interactions as ω_{pi}, where i = 1, 2, 3, ... corresponds to increasing separation $d_i = a, \sqrt{2}a, 2a$, ... for NN, second NN (2NN), third NN (3NN), ... 4fh sites. Thus, in terms of this general notation, ω_{p1} replaces the previous notation ω_{NN} introduced in section 2.1 for the Ising lattice-gas model. Trio interactions will be labeled as ω_{ti}, where i = 1, 2, 3, ... corresponds to increasing perimeter length, p_i, of the trio motif. For linear motifs, p_i is taken as twice the length. Thus, one has $p_1 = (2 + \sqrt{2})a$ for a bent trio, $p_2 = 4a$ for a linear trio, etc. Quarto interactions could be denoted by ω_{qi} where perimeter length p_i increases with i and $p_1 = 4a$ for a square motif. The expectations from previous analysis for homoepitaxial transition-metal systems is that attractive (negative) ω_{p1} will dominate, attractive ω_{p2} and repulsive (positive) ω_{t1} generally being the next strongest interactions, and other ω's being smaller in magnitude.[32,37,50] Another expectation is that the magnitude of these interactions will decrease with increasing i, although oscillatory decay is possible.[24,30,51]

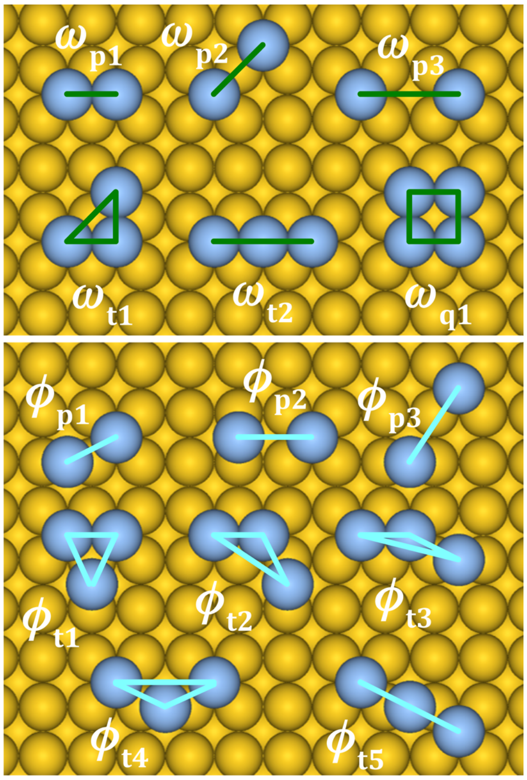

Figure 3. Conventional ω-interactions (top) and unconventional ϕ-interactions (bottom).

Below, E_ν will denote the total (adsorption + lateral interaction) energy per adatom for various periodic adlayer orderings ν = p(1 × 1), c(2 × 2), etc. Selected DFT results for E_ν using the PBEsol functional are shown in Table 3 for Ag and Cu. The adsorption energy, E_{4fh}, of isolated adatoms at 4fh sites is obtained by choosing $\nu = p(n \times n)$, for sufficiently large n. More generally, $E_\nu - E_{4fh}$ corresponds to the total lateral interaction energy per adatom for ordering ν, which can be expanded in terms of the ω's. For example, listing explicitly contributions from ω_{p1}, ω_{p2}, ω_{t1}, ω_{t2}, and ω_{q1}, while leaving other ω's implicit, one has that

Table 3. Key PBEsol Energies E_ν (in eV) for Ag(100) and Cu(100)

	$E_{p(4\times4)}$	$E_{p(2\times2)}$	$E_{(4\times4)\text{-NN}}$	$E_{(3\times3)\text{-2NN}}$	$E_{c(2\times2)}$	$E_{p(1\times1)}$
Ag	−2.543	−2.524	−2.689	−2.556	−2.599	−3.074
Cu	−3.320	−3.310	−3.511	−3.354	−3.429	−4.028

$$E_{p(1\times1)} - E_{4fh} = -2\omega_{p1} - 2\omega_{p2} - ... - 4\omega_{t1} - 2\omega_{t2} - ... - \omega_{q1} - ... \tag{2}$$

$$E_{c(2\times2)} - E_{4fh} = -2\omega_{p2} - ... \tag{3}$$

etc., and it is natural to define an effective NN pair interaction $\omega_{p1}^{eff} = [E_{p(1\times1)} - E_{4fh}]/2$, which contains contributions from all ω's.

Of particular relevance for our modified strategy to determine ω's is that the key quantities related to step-edge thermodynamics described in section 2 can also be expressed in terms of these ω's. Specifically, one has

$$a\beta_{\langle110\rangle} = -\frac{1}{2}\omega_{p1} - \omega_{p2} - ... - 2\omega_{t1} - \omega_{t2} - ... - \frac{1}{2}\omega_{q1} - ... \tag{4}$$

$$\sqrt{2}\,a\beta_{\langle100\rangle} = -\omega_{p1} - \omega_{p2} - ... - 3\omega_{t1} - 2\omega_{t2} - ... - \omega_{q1} - ... \tag{5}$$

$$\Delta E_{\langle110\rangle} = -2\omega_{p1} - 0\omega_{p2} - ... - 4\omega_{t1} - 3\omega_{t2} - ... - 2\omega_{q1} - ... \tag{6}$$

$$\Delta E_{\langle100\rangle} = -0\omega_{p1} - 2\omega_{p2} - ... - 2\omega_{t1} - 0\omega_{t2} - ... - 0\omega_{q1} - ... \tag{7}$$

and

$$E_e^{form} = -\omega_{p1} - 0\omega_{p2} - ... - 2\omega_{t1} - \omega_{t2} - ... - \omega_{q1} - ... \tag{8}$$

where eqs 4 and 5 apply strictly at T = 0 K. From eqs 6 and 8, one has

$$\varepsilon_k = \frac{1}{4}\Delta E_{\langle110\rangle} = \frac{1}{2}E_e^{form} + \frac{1}{4}\omega_{t2} + ... \approx \frac{1}{2}E_e^{form} \tag{9}$$

given that ω_{t2} and other interactions not shown explicitly in the above equations are expected to be smaller in magnitude than ω_{p2} and ω_{t1} (and far below ω_{p1}). Thus, $E_e^{form} \approx \frac{1}{2}\Delta E_{\langle110\rangle}$ is largely determined by $\Delta E_{\langle110\rangle}$. Similarly, from eqs 4, 6, and 7, one has that

$$a\beta_{\langle 110\rangle} = \frac{1}{4}\Delta E_{\langle 110\rangle} + \frac{1}{2}\Delta E_{\langle 100\rangle} - \frac{1}{4}\omega_{t2} + \ldots \qquad (10)$$

so that $\beta_{\langle 110\rangle}$ is largely determined by $\Delta E_{\langle 110\rangle}$ and $\Delta E_{\langle 100\rangle}$ for small ω_{t2}.

3.2. Determination of ω-Interactions.

While models retaining more conventional ω-interactions will generally be more accurate, tailored models with a smaller number of effective interactions might provide greater insight into the key parameters controlling behavior. From this perspective, it is instructive to discuss construction of a sequence of models (Cn) retaining n independent ω's for n = 1, 2, 3, and 4. We also contrast the determination of these ω's from a standard CE-type approach with that from our alternative approach recovering key step-edge thermodynamics. For both approaches, we identify E_{4fh} for isolated atoms as $E_{p(n\times n)}$ for n = 2, anticipating that relaxation in such smaller unit cells will be closer to that for typical step-edge configurations than for n = 4. Below we refer to "true" values of ω_{p1} and ω_{p2}. The "true" ω_{p1} is determined from $E_{(4\times4)\text{-NN}} \approx E_{4fh} + \omega_{p1}/2$, where ν = (4 × 4)-NN contains an isolated NN ad-dimer in a 4 × 4 unit cell. The "true" ω_{p2} is estimated from $E_{(3\times3)\text{-2NN}} \approx E_{4fh} + \omega_{p2}/2$, where ν = (3 × 3)-2NN contains an isolated 2NN ad-dimer in a 3 × 3 unit cell.

C1 Model Retaining $\omega = \omega_{p1}$. A standard approach might determine ω_{p1} from the energetics of a complete p(1 × 1) adlayer, that is, $\omega_{p1} = [E_{p(1\times1)} - E_{4fh}]/2 = \omega_{p1}^{\text{eff}}$. Such a model will capture the critical temperature below which one has 2D phase separation and island formation.[28] Our alternative strategy captures exactly the edge adatom creation energy, and thus instead sets $\omega_{p1} = E_e^{\text{form}}$. This Ising-type C1 model cannot recover the relative magnitudes of step energies or stiffness for ⟨110⟩ and ⟨100⟩ orientations, as has been discussed extensively for Cu(100).[52−55]

C2 Model Retaining ω_{p1} and One of ω_{p2} or ω_{t1}. Retaining one of ω_{p2} or ω_{t1} is perhaps not so appealing as they are expected to have comparable magnitudes (which exceeds that of longer-range pair and other trio interactions). Nonetheless, we consider a somewhat standard approach, in which the "true" attractive ω_{p1} is determined directly from analysis of an isolated ad-dimer in a large unit cell. The second ω extracted from $E_{p(1\times1)}$ then will be repulsive for Ag and Cu because we find that $[E_{p(1\times1)} - E_{4fh}] + 2\omega_{p1} > 0$. Thus, one naturally retains ω_{t1} whose true value is expected to be repulsive.

Our alternative approach selects ω's to recover both $\Delta E_{\langle 110\rangle}$ and $\Delta E_{\langle 110\rangle}$, thus capturing aspects of the anisotropy in step thermodynamics, as well as recovering $E_e^{\text{form}} \approx \Delta E_{\langle 110\rangle}/2$. This yields a strong attractive ω_{p1} and a weak attractive second ω, which is thus naturally selected as ω_{p2}. Indeed, it was observed that a model including ω_{p1} and ω_{p2} yields significant improvements over an Ising-type C1 model for Cu(100) step-edge properties,[54,55] although this model still has shortcomings.[24,27,44]

C3 Model Retaining ω_{p1}, ω_{p2}, and ω_{t1}. This model is appealing as it retains the three interactions expected to have the largest magnitudes. A standard CE-type approach might again determine the "true" ω_{p1} directly from analysis of an isolated ad-dimer in a large unit cell, and then determine ω_{p2} and ω_{t1} from E_ν for two other ν's, say, p(1 × 1) and c(2 × 2). We find that such an analysis automatically generates the expected sign and magnitude for these interactions. Our alternative approach retains the "true" ω_{p1} and chooses the other ω's to recover both $\Delta E_{\langle 110\rangle}$ and $\Delta E_{\langle 100\rangle}$.

C4 Model Retaining ω_{p1}, ω_{p2}, ω_{t1}, and ω_{t2}. Previous C4-level modeling of metal (100) systems adopting a standard CE-type approach has retained this set of four ω's.[37,38] In this work, we will implement an alternative strategy, which uses the "true" values of ω_{p1} and ω_{p2} from large unit cell calculations, and then determine ω_{t1} and ω_{t2} to recover both $\Delta E_{\langle 110\rangle}$ and $\Delta E_{\langle 110\rangle}$.

Results for our estimates of ω's for Cn models are shown in Table 4 for both standard (std) and alternative (alt) approaches. We believe that the values are reasonable by comparison with previous studies,[37,50] and also by comparison with selected direct calculations for Ag in section S4.

Table 4. PBEsol Estimates of ω-Interactions (in eV) for Cn Models from Standard (std) and Alternative (alt) Approaches for Ag(100) and Cu(100)

			ω_{p1}	ω_{p2}	ω_{t1}	ω_{t2}
Ag	C1	std	−0.275			
		alt	−0.239			
	C2	std	−0.329		+0.027	
		alt	−0.241	−0.010		
	C3	std	−0.329	−0.037	+0.045	
		alt	−0.329	−0.054	+0.044	
	C4	alt	−0.329	−0.063	+0.052	−0.011
Cu	C1	std	−0.359			
		alt	−0.303			
	C2	std	−0.402		+0.021	
		alt	−0.296	−0.024		
	C3	std	−0.402	−0.060	+0.051	
		alt	−0.402	−0.077	+0.053	
	C4	alt	−0.402	−0.089	+0.065	−0.016

In closing, we note that there are other ways to characterize the energetics controlling adlayer thermodynamics instead of decomposition in terms of ω's. The so-called connector model is one such general approach.[56] Another alternative geared to step-edge thermodynamics at the C2 level retains ω_{p1}, but introduces an effective corner or kink energy in place of ω_{p2}.[57]

4. UNCONVENTIONAL LATERAL ADATOM ϕ-INTERACTIONS

4.1. ϕ-Interactions and Step-Edge Diffusion Barriers.

First, we discuss selection and determination of unconventional ϕ-interactions. As indicated in the bottom panel of Figure 3, we label pair interactions as ϕ_{pi}, where i = 1, 2, 3, ... corresponds to increasing separation $d_i = \sqrt{5}a/2 \approx 1.118a$, $3a/2 = 1.5a$, $\sqrt{13}a/2 \approx 1.803a$, ... Trio interactions will be labeled as ϕ_{ti}, where i = 1, 2, 3, ... corresponds to increasing perimeter length, p_i, of the trio motif: $p_1 = (1 + \sqrt{5})a \approx 3.236a$ for a triangular trio, $p_2 = (1 + \sqrt{5/2} + \sqrt{13/2})a \approx 3.921a$, and $p_3 = (1 + \sqrt{5/2} + \sqrt{17/2})a \approx 4.180a$ for a bent trio with a "terminal" adatom at the bridge site. These interactions are important for description of PD around adatom islands and associated sintering. In addition, we will consider unconventional interactions labeled ϕ_{t4} and ϕ_{t5} with $p_4 = (2 + \sqrt{5})a \approx 4.236a$ and $p_5 = 2\sqrt{5}a \approx 4.472a$ for trios with a "central" adatom at the bridge site. As discussed below, these ϕ-interactions will be important for description of sintering of pits. The expectation from limited previous analysis[37] is that strong attractive ϕ_{p1} and weaker repulsive ϕ_{t1} will dominate other interactions. Another default expectation is that the magnitude of at least the pair interactions will decrease with increasing i.

As noted in section 1, from these ϕ's, we can determine Φ_{TS} for various edge diffusion processes. The corresponding barriers then follow from eq 1 after determining E_d and the relevant Φ_{init}. In the expressions below, we just list explicitly the ϕ's shown in Figure 3, and leave the others implicit. For example, for diffusion along straight close-packed ⟨110⟩ edges, one has that

$$\begin{aligned} E_e = {} & E_d + (2\phi_{p1} + 2\phi_{p3} + \ldots + \phi_{t1} + 2\phi_{t2} + 2\phi_{t3} + \ldots) \\ & - (\omega_{p1} + 2\omega_{p2} + \ldots + 2\omega_{t1} + \omega_{t2} - \ldots - 0\omega_{q1} - \ldots) \end{aligned} \tag{11}$$

The additional barrier, δ_{kr}, for edge atoms to round kinks or corners is given by

$$\delta_{kr} = -\phi_{p1} - 3\phi_{p3} - \ldots - \phi_{t1} - \phi_{t2} - \phi_{t3} - \ldots \tag{12}$$

The barrier, E_m, for extraction from ⟨100⟩ step edges, which impacts step meandering kinetics, is given by

$$\begin{aligned} E_m = {} & E_d + (2\phi_{p1} + \phi_{p2} + \phi_{p3} + \ldots + \phi_{t1} + \phi_{t2} + 2\phi_{t3} \\ & + \ldots) \\ & - (2\omega_{p1} + 3\omega_{p2} + \ldots + 5\omega_{t1} + 2\omega_{t2} - \ldots - \omega_{q1} - \ldots) \end{aligned} \tag{13}$$

The barrier, E_b, for breakout from a close-packed ⟨110⟩ step edge is given by

$$\begin{aligned} E_b = {} & E_d + (2\phi_{p1} + \ldots + 0\phi_{t1} + 2\phi_{t2} + 2\phi_{t3} + \phi_{t4} + 0\phi_{t5} \\ & + \ldots) \\ & - (3\omega_{p1} + 2\omega_{p2} + \ldots + 6\omega_{t1} + 4\omega_{t2} - \ldots + 2\omega_{q1} - \ldots) \end{aligned} \tag{14}$$

In this study, we consider sintering of single-atom-deep pits, as well as of adatom islands. Our formulation should also describe pit diffusion. In this context, one anticipates that a key edge diffusion process for pit configurations (which tend to exhibit concave step edges) involves sliding of an atom adjacent to the corner out along a ⟨110⟩ step edge; see Figure 2f. The barrier, E_s, for this sliding process is given by

$$\begin{aligned} E_s = {} & E_d + (3\phi_{p1} + \ldots + \phi_{t1} + 3\phi_{t2} + 3\phi_{t3} + \phi_{t4} + \phi_{t5} \\ & + \ldots) \\ & - (3\omega_{p1} + 3\omega_{p2} + \ldots + 7\omega_{t1} + 4\omega_{t2} - \ldots + 2\omega_{q1} - \ldots) \end{aligned} \tag{15}$$

It is appropriate to note that the unconventional interactions ϕ_{t4} and ϕ_{t5}, with the hopping atom at the bridge-site TS between two other atoms at 4fh sites, do not impact edge diffusion around convex islands. However, they do naturally impact diffusion at the edge of pits. They are also relevant for diffusion of single vacancies through islands, although they were not incorporated into previous modeling.[37] In addition, it should be also mentioned that the formulas for the barriers given above sometimes need modification to account for the smaller unit cells used in the DFT analysis.[37]

4.2. Determination of ϕ-Interactions. While models retaining more ϕ-interactions will be more accurate, again tailored models with a smaller number of effective interactions might provide useful insight. Thus, we discuss a sequence of models (Un) retaining n independent ϕ's for n = 1, 2, 3, and 4.

U1 Model Retaining a Single $\phi = \phi_{p1}$. In this model, it is natural to choose ϕ_{p1} to recover the exact value of the barrier, E_e, for diffusion along close-packed ⟨110⟩ steps. Note that this model will impose a kink-rounding barrier equal to $\delta_{kr} = -\phi_{p1} = |\phi_{p1}|$.

U2 Model Retaining Both ϕ_{p1} and ϕ_{t1}. These two ϕ's are expected to have the largest magnitude, so this model is appealing. Naturally, ϕ_{p1} and ϕ_{t1} are chosen here to recover both E_e and the additional kink-rounding barrier, δ_{kr}. Such a model, when combined with any Cn model recovering the exact value of E_e^{form}, should suffice to effectively describe adatom-island sintering.

U3 Model Retaining Independent ϕ_{p1}, ϕ_{t1}, and ϕ_{t3} (and Dependent ϕ_{t2}). A previous study[37] suggested that longer-range pair interactions, ϕ_{pi}, with $i > 1$, are small. This study also indicated that the values of trio interactions, $\phi_{ti=1,2,3}$, vary smoothly with the angle of the trio motif from repulsive values for a triangular motif of ϕ_{t1} to attractive for a close-to-linear motif of ϕ_{t3}. Thus, we adopt a weighted average for $\phi_{t2} = \eta\phi_{t3} + (1 - \eta)\phi_{t1}$ with fixed η close to unity as ϕ_{t2} is closer to ϕ_{t3} than ϕ_{t1}.[37] The three independent ϕ's are selected to recover all of E_e, E_{kr}, and E_m.

U4 Model Retaining Independent ϕ_{p1}, ϕ_{t1}, ϕ_{t3}, ϕ_{t4} (and Dependent ϕ_{t2}). We expect that reliable description of pit diffusion and sintering also requires recovery of the barrier, E_s, for sliding at pit corners. This E_s involves the combination $\phi_{t4} + \phi_{t5}$, where ϕ_{t4} and ϕ_{t5} have the bridge-site adatom between two other atoms at 4fh sites; see Figure 3. Limited direct calculations of these ϕ's indicate that ϕ_{t4} dominates ϕ_{t5}, so in our simulation analysis, we will set $\phi_{t5} = 0$. We note that expressions for E_e, E_{kr}, and E_m do not involve ϕ_{t4} or ϕ_{t5}.

Next, we present results for ϕ-interactions based on Cn + Un models for n = 1, 2, 3, and 4, specifically using ω-interactions from our alternative version of Cn incorporating step-edge thermodynamics. The results of ω-interactions from our alternative version of Cn used to obtain ϕ-interactions of Un have been presented in Table 4. In addition, in this analysis, we use our DFT results for E_d, E_e, E_{kr}, E_m, and E_s presented in Table 2. For C1 + U1, one simply uses the relation:

$$E_e \approx E_d + 2\phi_{p1} - \omega_{p1} \tag{16}$$

to obtain $\phi_{p1} = -0.243$ (−0.292) eV for Ag (Cu). For C2 + U2, one uses the relations:

$$E_e \approx E_d + 2\phi_{p1} + \phi_{t1} - \omega_{p1} - 2\omega_{p2} \tag{17}$$

and

$$\delta_{kr} \approx -\phi_{p1} - \phi_{t1} \tag{18}$$

to obtain $\phi_{p1} = -0.265$ (−0.312) eV and $\phi_{t1} = +0.022$ (+0.002) eV for Ag (Cu). For C3 + U3, one uses correspondingly more complex relations for E_e, δ_{kr}, and E_m involving independent ϕ_{p1}, ϕ_{t1}, and ϕ_{t3} (and dependent ϕ_{t2}) and 3 C3 ω's. For C4 + U4, the analysis for ϕ_{p1} and $\phi_{ti=1,2,3}$ is as for C3 + U3 but with 4 C4 ω's, and ϕ_{t4} follows from knowledge of E_s. Results for various Cn + Un models are shown in Table 5. Values appear reasonable by comparison with selected direct analyses for Ag in section S4.

5. OTHER LOW-STRAIN METAL (100) SYSTEMS

As noted in section 1, extensive systematic studies of nanocluster reshaping in metal (100) systems are available only for Ag/Ag(100). Limited qualitative observations are

Table 5. PBEsol Estimates of ϕ-Interactions (in eV) for Cn + Un Models for Ag(100) and Cu(100)[a]

		ϕ_{p1}	ϕ_{t1}	ϕ_{t2}	ϕ_{t3}	ϕ_{t4} + ϕ_{t5}
Ag	C1+ U1	−0.243				
	C2 + U2	−0.265	+0.022			
	C3 + U3	−0.207	+0.110	−0.058	−0.088	
	C4 + U4	−0.204	+0.121	−0.064	−0.096	+0.072
Cu	C1 + U1	−0.292				
	C2 + U2	−0.312	0.002			
	C3 + U3	−0.289	+0.104	−0.051	−0.078	
	C4 + U4	−0.285	+0.120	−0.058	−0.090	+0.074

[a] For U3 and U4, we have selected η = 0.85.

available for Cu/Cu(100). For this reason, we have focused on these two systems in sections 3 and 4. However, the formulation developed in this Article applies more generally to any metal (100) homoepitaxial systems, and also to low-strain metal (100) heteroepitaxial systems. There have been experimental studies for various homoepitaxial systems beyond Ag and Cu, including Pd, Ni, and Rh. Thus, we discuss related experimental results and present selected new DFT analysis relevant to NC sintering. Key features for a subset of the numerous systems discussed are summarized in Table 6.

Table 6. Summary for Various Homoepitaxial and Heteroepitaxial Systems of Model Applicability, Availability of STM Data for Sintering of Islands and/or Pits, and DFT Results for Dominant Terrace Diffusion Mechanism (Hopping versus Exchange)

systems	model applicability	STM data availability	hopping versus exchange
Ag/Ag(100)	yes	yes	hopping
Cu/Cu(100)	yes	yes	hopping
Ni/Ni(100)	yes	yes	exchange[a]
Pd/Pd(100)	yes	no	hopping
Rh/Rh(100)	yes	no	hopping[b]
Au/Ag(100)	yes	no	hopping
Ag/Fe(100)	yes	no	hopping
Pt/Pd(100)	no	no	exchange
Ir/Pd(100)	no	no	exchange
Ir/Rh(100)	no	no	exchange
Ta/Nb(100)	yes	no	hopping

[a] Experimental FIM[58] and DFT LDA studies[59] determine the terrace diffusion via exchange, but PW91[60] and our PBE analyses produce the terrace diffusion via hopping. [b] Experimental FIM studies confirm the terrace diffusion via hopping.[61]

5.1. Pd/Pd(100). Previous studies explored submonolayer island formation using surface-sensitive diffraction and suggested a diffusion barrier of around $E_d \approx 0.6$ eV assuming irreversible island formation at 300 K and a prefactor of $\nu \approx 5 \times 10^{12}$/s.[62] However, there are no existing experimental analyses of postdeposition island diffusion and coalescence. Subsequent DFT PW91 GGA analysis[63] assessed a hopping barrier of $E_d \approx 0.71$ eV. This analysis also indicated a slightly higher barrier of 0.82 eV for terrace diffusion via exchange with an underlying atom in the surface layer. A DFT LDA study estimated $E_d \approx 0.87$ eV for hopping and 0.85 eV for exchange,[64] but did not address the discrepancy with ref 63 or experiment. Using a 15-ML slab and 4 × 4 unit cell, we perform the DFT analyses for E_d. Our PBE value of E_d is consistent with $E_d \approx 0.71$ eV in ref 63, but our PBEsol value is ~0.1 eV larger than the PBE value. We go further to determine edge diffusion and kink-rounding barriers. See Table 7 for our DFT results of these key barriers.

Table 7. DFT PBEsol Estimates of Activation Barriers (in eV) for Key Diffusion Processes for Pd/Pd(100)

E_d (hop)	E_d (exchange)	E_e	δ_{kr}	E_{kr}
0.818	0.887	0.449	0.370	0.819

We also determine $E_{4fh} \approx E_{p(4\times4)} = -3.825$ eV, $E_{p(4\times4)\text{-NN}} = -3.968$ eV, and $E_{p(1\times1)} = -4.473$ eV, so that the "true" $\omega_{p1} = 2[E_{p(4\times4)\text{-NN}} - E_{4fh}] = -0.286$ eV and $\omega_{p1}^{eff} = [E_{p(1\times1)} - E_{4fh}]/2 = -0.324$ eV from PBEsol analyses. For more details of the calculations, see the Supporting Information.

5.2. Ni/Ni(100). STM studies explored submonolayer island formation,[65] analysis of which indicated a lower bound on E_d of around 0.45 eV.[28] Separate STM studies examined pit evolution and coalescence for coverages near 1 ML.[66] Field-ion microscopy (FIM) studies directly determined that terrace diffusion occurred via exchange with E_d = 0.63 eV.[58] An earlier PW91 analysis just determined E_d = 0.72 eV for hopping.[60] A subsequent analysis[59] emphasized that the LDA exchange barrier of E_d = 0.78 eV was somewhat below the LDA hopping barrier of 0.82 eV, consistent with the above experimental result of more favorable exchange than hopping. Reference 59 did not elucidate the discrepancy between the experimental E_d = 0.63 eV and their DFT values: LDA E_d = 0.82 (0.78) eV for hopping (exchange); PW91 E_d = 0.72 (0.77) eV for hopping (exchange). Our own PBE analysis (using a 4-ML slab and 10 × 10 unit cell) produces E_d = 0.729 eV for hopping and E_d = 0.817 eV for exchange, comparable to previous PW91 results.[60] While terrace diffusion occurs via exchange, we believe our model for PD-mediated reshaping via hopping is still applicable. The key point is that although exchange is favored on the terrace, this pathway is expected to be strongly inhibited at step edges given the crystalline geometry.

5.3. Other M/M(100) Systems. We more briefly remark on some other homoepitaxial systems where our modeling should apply. For Rh/Rh(100), there are currently no experimental studies for submonolayer island formation or postdeposition coalescence. However, experimental FIM studies have confirmed that terrace diffusion occurs via hopping with a barrier of 0.88 eV,[61] quite consistent with a PW91 estimate of E_d = 0.89 eV.[60] There are extensive studies of submonolayer island formation for Fe/Fe(100).[67] However, we find that DFT analysis for this bcc system produces some special challenges, which will be discussed in a separate publication. We have also performed DFT analyses for two other bcc metals. We find that PBE analysis (using a 5-ML slab and 4 × 4 unit cell) produces E_d = 0.883 (1.664) eV for hopping (exchange) for Nb/Nb(100); E_d = 1.099 (1.687) eV for hopping (exchange) for Ta/Ta(100).

Next, we provide several examples, which address the applicability of our stochastic lattice-gas-modeling approach for NC reshaping for low-strain heteroepitaxial metal (100) systems.

5.4. Au/Ag(100). This system has negligible lateral strain because fcc Au and fcc Ag have almost identical bulk lattice constants. Previous experiments of few-layer growth focused on electronic properties, but suggested island formation and smooth growth at 300 K.[68] Previous DFT analysis[37,38] indicated a terrace-diffusion barrier via hopping of $E_d \approx 0.53$ eV from

PBE. Regarding exchange of Au with Ag in the top surface layer, this process was found to be roughly energy-neutral and occurs with a barrier around 0.18 eV higher than terrace diffusion.[37] Consequently, this exchange process is not significant below 300 K, and our model applies.

5.5. Ag/Fe(100). Another system with excellent lattice-match is Ag on bcc Fe(100), where previous experimental studies have focused on few-layer growth.[69,70] In this case, DFT analysis indicates a terrace-diffusion barrier via hopping of $E_d \approx$ 0.39 eV from PBE, with a significant energy cost for Ag to exchange with Fe in the top surface layer.[51] Thus, this exchange process is not significant and our model applies.

5.6. Pt/Pd(100). Given that fcc Pt and fcc Pd also have similar bulk lattice constants, it is also natural to consider Pt/Pd(100). Experimental studies have been performed for the T-dependence of few-layer growth in this system, assessing the onset temperature for surface diffusion, which was assumed to be Pt hopping on Pd(100).[71] Another study assessed the onset of reconstruction of the (100) surface of a Pt thin film, again assuming no significant intermixing.[72] More recent studies have explored the solution-phase epitaxial growth of Pt on Pd nanocubes with exposed (100) facets.[73] We have performed a DFT analysis using PBE for this system (using a 4-ML slab and 4 × 4 unit cell) to obtain E_d = 0.978 eV for hopping versus much lower E_d = 0.596 eV for exchange. Furthermore, we find that the system energy is lowered by 0.389 eV during the exchange process; that is, exchange and associated intermixing are thermodynamically preferred. As a result, our model with just hopping diffusion is not appropriate for analysis of this system. Furthermore, we conclude that the key surface diffusion process controlling film-growth morphology in the study of ref 71 was presumably not Pt hopping on Pd(100). This propensity for Pt exchange with Pd(100) was recently recognized and analyzed in ref 73, which reported E_d = 0.99 eV for hopping and E_d = 0.74 eV for exchange with an energy reduction from exchange of 0.38 eV. Their higher estimate for the exchange barrier is undoubtedly due to the feature that only a 3 × 3 unit cell was used constraining the movement of atoms during the exchange process.

5.7. Ir/Rh(100) and Ir/Pd(100). Fcc Ir has a bulk lattice constant similar to those of both fcc Rh and fcc Pd(100). For Ir/Rh(100), our PBE analysis (using a 5-ML slab and 4 × 4 unit cell) yields E_d = 1.100 eV for hopping versus lower E_d = 0.876 eV for exchange. Furthermore, we find that the system energy is lowered by 0.514 eV during exchange; that is, intermixing is thermodynamically preferred. For Ir/Pd(100), our PBE analysis (using a 4-ML slab and 4 × 4 unit cell) yields E_d = 1.267 eV for hopping, but a strong preference for intermixing with the energy lowered by 1.037 eV via exchange. Our cNEB calculation indicates a barrier for intermixing of below 0.3 eV. Thus, again our model with just hopping diffusion is not appropriate.

5.8. Ta/Nb(100) and Nb/Ta(100). Bcc Ta and bcc Nb also have essentially identical bulk lattice constants. Our PBE analysis (using a 5-ML slab and 4 × 4 unit cell) produces E_d = 1.010 eV for hopping and E_d = 1.613 eV for exchange for Ta/Nb(100) (with exchange thermodynamically favored by 0.221 eV); E_d = 0.992 eV for hopping and E_d = 1.783 eV for exchange for Nb/Ta(100) (where exchange is not preferred thermodynamically). Even for Ta/Nb(100), there will be a window of temperature where hopping is active but not exchange, so our modeling will be applicable.

Finally, we note that Ag/Au(100), Pd/Pt(100), and Rh/Ir(100) are not considered above due to the hex-reconstruction of (100) surfaces of Au, Pt, and Ir, which is not incorporated into our model. On the other hand, our model does naturally extend to treat low-strain codeposition systems on metal (100) surfaces without reconstruction or significant intermixing, for example, (Au + Ag)/Ag(100),[37] (Ag + Fe)/Fe(100), or (Nb + Ta)/Ta(100).

6. KMC SIMULATION STUDIES: SINTERING OF ISLANDS AND PITS ON Ag(100)

Much previous modeling of NC restructuring and diffusion has tended to use simple generic models and to address general issues rather than make system-specific predictions. Our goal here is to demonstrate the predictive capability of our detailed model incorporating ab initio thermodynamics and kinetics. As systematic and comprehensive experimental analysis of NC sintering is available only for Ag/Ag(100) at 295 K,[2,4,39] we consider this case. The requirement is not just to recover the characteristic time, τ, for sintering for a selected case such as that shown in Figure 1, but also to recover the strong dependence of τ on the characteristic linear size, L_c, of the constituent NCs. For the latter, it should be emphasized that the classic prediction of a continuum theory, $\tau \approx (L_c)^4$, is not expected to apply on the nanoscale.[2,13,23] All following simulations of island sintering are performed by utilizing our most detailed C4 + U4 model.

Below, if two near-square or more generally near-rectangular clusters sizes are $L_{x1} \times L_{y1}$ and $L_{x2} \times L_{y2}$, we define the characteristic size $L_c = \sqrt{(L_{x1}L_{y1} + L_{x2}L_{y2})/2}$. It should also be noted that the dimensions L_{xi} and L_{yi}, where i labels the NC, denote the size of a rectangle, which circumscribes the NC, so the actual area is smaller than $L_{xi}L_{yi}$ because the NC has "rounded corners". We will take into account this feature when comparing STM data with KMC simulations. We also note that the experimental surface lattice constant for Ag(100) is a = 0.289 nm.[74]

Postdeposition analysis of submonolayer island distributions for Ag/Ag(100) at 295 K reveals coarsening by Smoluchowski ripening (NC diffusion and coalescence).[1] One can find multiple examples of roughly corner-to-corner collision and coalescence of islands or NCs. From these, we mainly select those cases where the two NCs have roughly equal size. Such an example is shown in Figure 1 comparing STM data (top) and KMC simulations (bottom) for sintering at 295 K where the two clusters have sizes of 7.3 × 7.0 and 7.9 × 7.6 nm^2 prior to coalescence, so $L_c \approx$ 7.45 nm. Our KMC simulations mimicking this case start with 24 × 25 and 27 × 27 atom NCs, which reasonably match the rectangular envelope of the experimental clusters given that a = 0.289 nm. The two actual initial clusters are well-described by truncating the corners of the square or rectangular envelope with long ⟨110⟩ edges to generate short ⟨100⟩ edges. The relative length of the two types of edges is determined by $\beta_{\langle 110\rangle}/\beta_{\langle 100\rangle} < 1$ in the limit of large sizes. Thus, we truncate the corners of the 24 × 25 and 27 × 27 atom NCs by removing 3 and 4 atoms, respectively, and join the truncated clusters corner-to-corner along the ⟨100⟩ edge at simulation time t = 0. Other cases described below are treated in an analogous fashion (with larger numbers of corner atoms removed for larger NCs). Our simulation model reliably captures the time scale and morphological evolution of these NC pairs.

DOI: 10.1021/acs.jpcc.6b07328
J. Phys. Chem. C 2016, 120, 21617−21630

Next, we assess the NC size-dependence of sintering. Figure 4 shows the sintering behavior for a sequence of NC pairs of increasing size $L_c \approx 4.86$, 6.25, 8.44, and 12.27 nm comparing STM data (Figure 4a,c,e,g) with the corresponding KMC simulations (Figure 4b,d,f,h), respectively. The time scale for sintering significantly increases with increasing L_c by roughly an order of magnitude over this range. Our simulation model recovers the sintering times in all cases, thus effectively describing this nontrivial size-dependence. Note that in one (Figure 4e,f) of these cases, the two initial clusters have significantly different sizes, but in the other cases they are quite close in size.

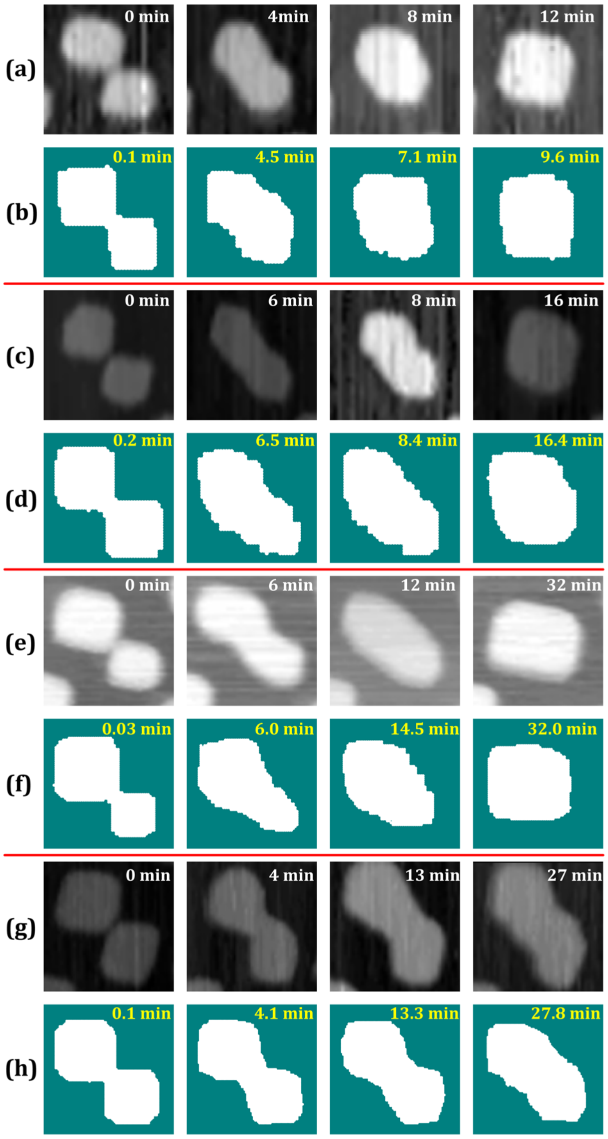

Figure 4. Examples of corner-to corner sintering of Ag NC pairs on Ag(100) at 295 K. NC sizes: (a,b) 5.2×5.2 nm^2 + 4.5×4.5 nm^2, $L_c \approx 4.86$ nm; (c,d) 6.5×6.5 nm^2 + 6.0×6.0 nm^2, $L_c \approx 6.25$ nm; (e,f) 10.8×9.0 nm^2 + 8.4×5.4 nm^2, $L_c \approx 8.44$ nm; (g,h) 13.0×13.0 nm^2 + 11.5×11.5 nm^2, $L_c \approx 12.27$ nm. (a), (c), (e), and (g) show STM images, and (b), (d), (f), and (h) show the corresponding KMC simulation results.

A quantitative analysis requires more precise definition of the sintering time. We mention three choices: (i) One imprecise possibility is to consider the time, τ_{sq}, to achieve a near-square shape. There is some uncertainty as to the initial collision time in the STM data, although this can usually be determined to within 1 min. However, a key need is to prescribe the condition for near-squareness. A natural choice comes from recognizing that in the later stages of sintering the coalesced NC pair achieves a convex shape. The longest dimension is along the line through the centers of the initial NCs, and the shortest is in the orthogonal direction. One can specify that a near-square shape is achieved when the shortest dimension is, say, 90% of the longest. (ii) A more convenient alternative is to consider the time, τ_{cx}, for the coalesced NC pair to achieve a convex shape. (iii) Another choice avoiding the uncertainty in collision time in STM data is to consider the time, τ_{neck}, for the width of the neck region to grow from, say, $L_c/2$ to L_c.

Table 8 summarizes results for various sintering times from STM and KMC analysis for a range of NC sizes, where these estimates come from analysis of additional images not shown in Figures 1 and 4. It is clear that $\tau_{sq} > \tau_{cx} > \tau_{neck}$, but we do not show results for the latter given the large uncertainty in measurement. In fact, we emphasize that large fluctuations in shape evolution for small NC sizes considered here preclude precise determination of any of these τ's from a single experiment or simulation. These large uncertainties are reflected in the values in Table 8. It should be mentioned that one could perform many simulation trials for the same initial conditions and average, but we do not pursue such analysis here. Nonetheless, as noted above, τ exhibits a clear increase with increasing L_c. Fitting the most reliable KMC data for τ_{cx} indicates that $\tau_{cx} \approx (L_c)^n$ with $n \approx 2.6$ well below the above-mentioned continuum prediction of $n_c = 4$. Fitting STM data for τ_{cx} and KMC data for τ_{sq} leads to similar estimates of $n \approx 2$–2.5. Such values well below $n_c = 4$ are expected given the small size of the NCs and presence of a substantial additional kink-rounding barrier. Note that for Ag/Ag(100), the additional kink-rounding barrier is $\delta_{kr} = 0.233$ eV from Table 2, so that the corresponding kink Ehrlich–Schwoebel length $L_{kr} = a\,e^{\delta_{kr}/(k_BT)} \approx 2.8$ μm far exceeds L_c (the condition for breakdown of the continuum theory[13]).

As indicated in section 1, one can in principle assess sintering not just of single-atom-high islands, but also of single-atom-deep pits on Ag(100). There are no available STM observations of sintering of pits in the size range considered above for islands, so corresponding direct comparison of experiment with KMC simulations of our model is not possible. However, there are limited observations of the sintering of larger pits (still with

Table 8. Sintering Times (in min) from KMC Simulation (STM Experiment)

	L_c (nm)				
	4.86	6.25	7.45	8.44	12.27
τ_{sq}	≳8 (∼12)	≳18 (∼14)	≳26 (∼20–25)	≳28 (∼25–30)	∼90 (??[a])
τ_{cx}	3–4 (∼6)	7–9 (∼9)	7–12 (∼11)	8–14 (∼12)	45 (∼40)

[a] No experimental data available.

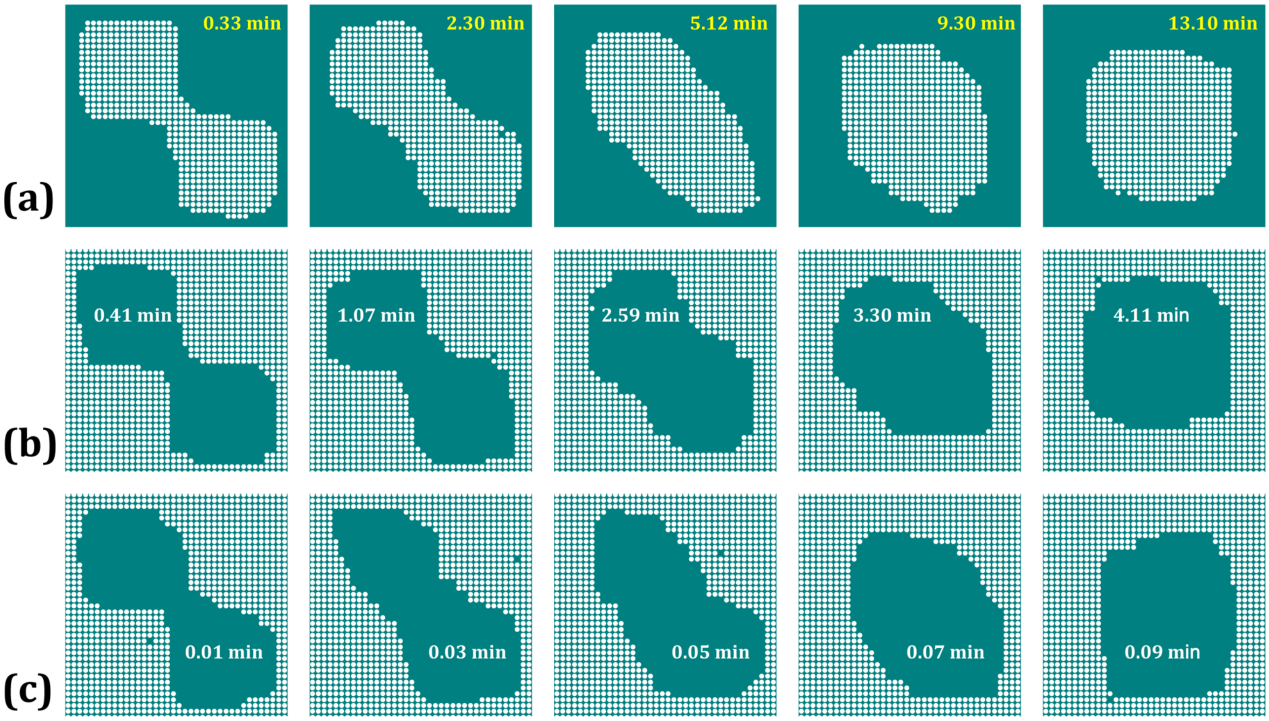

Figure 5. Comparison of KMC simulation results at 295 K for corner-to-corner sintering of (a) two 17 × 17 atom islands, and (b) two 17 × 17 vacancy pits. Cases (a) and (b) utilize our complete C4 + U4 model. Case (c) sets $\phi_{t4} = \phi_{t5} = 0$.

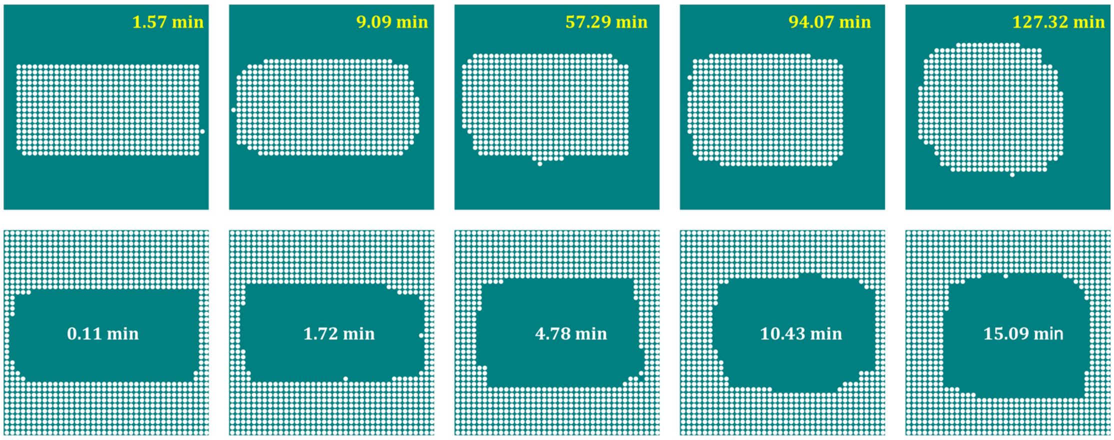

Figure 6. Comparison of KMC simulation results at 295 K from our C4 + U4 model for evolution of (a) a 34 × 17 atom island, and (b) a 34 × 17 vacancy pit.

L_c well below L_{kr}),[2] and of reshaping of more irregular pit structures,[23] which suggest a sintering time on the same order of magnitude as that for islands of comparable size. Thus, it is natural to compare predicted behavior of our stochastic model for sintering of islands and pits, noting that previous atomistic simulations of pit sintering are limited.[23] To this end, we compare benchmark simulations for sintering of two 17 × 17 atom (4.9 × 4.9 nm^2) islands and pits as shown in Figure 5. Results using our most detailed C4 + U4 model are shown in Figure 5a for islands and in Figure 5b for pits. The sintering time for pits is somewhat shorter than that for islands (by a factor of ~3), but this appears consistent with the limited experimental observations. However, additional insight into this behavior comes from examining the predictions of a refined simulation model where we "switch off" the unconventional repulsive interaction $\phi_{t4} = 0$ (and also set $\phi_{t5} = 0$). The corresponding simulation results shown in Figure 5c reveal much faster pit sintering (by a factor of more than 100 relative to island sintering), which is not compatible with experiment. Setting $\phi_{t4} = \phi_{t5} = 0$ significantly lowers the barrier of the corner sliding process relative to that in the full C4 + U4 model, and greatly accelerates the overall pit sintering process. Thus, this study serves to emphasize the importance of incorporating realistic values for such unconventional interactions. Finally, as an aside, we note that there has been an experimental study of pit sintering on Ag(111) surfaces for which the scaling of relaxation time with pit size was also considered.[75]

Next, with regard to these benchmark simulations, we have also tested the effectiveness of our simpler C2 + U2 model for predicting island sintering. As suggested in section 4, the success of this simpler model is expected because it incorporates exact edge-diffusion and corner-rounding rates. Indeed, simulated island evolution is comparable to that using the more detailed C4 + U4 model. On the other hand, this simplified model fails to recover the behavior predicted by our C4 + U4 model for pit sintering, predicting too rapid sintering by a factor of about 3.

Finally, we note that STM studies do reveal some limited examples of side-by-side (relative to corner-to-corner) sintering. Typically, the NCs that collide side-to-side do not have exactly the same size and there is a fast reshaping of the coalesced NCs removing any concave regions to achieve a near-rectangular shape; see Figure 1c of ref 2. Subsequently, there is a slower evolution of the near-rectangular shape toward a near-square shape. Note that this reshaping process (in contrast to corner-to-corner sintering) can be limited by nucleation of new outer edges on the long sides of the rectangle in the regime where $L_c \ll L_k$ (see section 2.3).[13−15] We perform benchmark simulations focused on the latter stage conversion of rectangles to squares, comparing behavior for islands and pits. Figure 6 shows the results at 295 K from KMC simulation using our C4 + U4 model, starting with (a) a 34 × 17 atom NC; and (b) a 34 × 17 atom vacancy pit (i.e., 9.8 × 4.9 nm^2). Results indicate that pit sintering is ∼10 times faster than island sintering in this size range. Very limited STM observations for larger sizes ∼28 × 15 nm^2 do suggest faster pit sintering (for the same size islands and pits),[2] although quantitative analysis is not viable.

7. DISCUSSION AND CONCLUSIONS

We have developed a general formalism to describe the shape evolution of 2D nanoislands and nanopits on unreconstructed metal (100) surfaces in cases where the process is mediated by PD, which in turn involves adatom hopping. The formalism is designed to incorporate both ab initio step-edge thermodynamics and kinetics in contrast to more generic modeling. A range of models is presented retaining different numbers of conventional ω-interactions and unconventional ϕ-interactions. Models retaining more interactions naturally give a more accurate description, but those with fewer can be crafted to capture key features of step-edge physics and potentially provide more insight into key parameters controlling behavior. The C4 + U4 model with 4 ω's and 4 ϕ's is perhaps the optimum choice.

The time scale for coalescence or sintering of NC pairs is extremely sensitive to barriers for PD and thus provides an ideal benchmark for DFT energetics. Our analysis reveals that PBEsol energetics is consistent with experimental observations for Ag(100), but not PBE energetics (for which the magnitude of adatom interactions and related quantities as well as of diffusion barriers is about 80% of PBEsol values).

Unfortunately for Cu(100), there is not any available quantitative experimental analysis of the coalescence of NC pairs. Certainly, our model predicts slower sintering for Cu(100) than for Ag(100) as a direct consequence of the higher value of the effective overall activation barrier E_{eff} (and of each of its constituent energies). Actually, qualitative experimental observations for Cu(100) do not give an indication of significantly slower reshaping than for Ag(100). However, Cu surfaces are more prone to impurities, for example, deriving from bulk S. Thus, it is perhaps possible that observed behavior is impacted by such effects. This view was recently considered in analysis of step flow on Cu(100).[76] Perhaps more relevant, we also mention that even trace amounts of S can greatly enhance decay of NCs on Cu(111) surfaces.[77,78]

From a broader perspective of shape evolution of both 2D and 3D NCs, a precise ab initio description of PD kinetics in all possible local environments is essential. This means, for example, discriminating between diffusion along straight edges in 2D (or on facets in 3D) and diffusion around kinks or corners in 2D (or between facets in 3D). Our general modeling framework including both conventional and unconventional interactions to reliably reconstruct PD barriers has general applicability.

It is natural to consider extension of this analysis to treat sintering of islands and pits on fcc (111) metal surfaces.[41,75,79] However, high-level treatment of kinetics in these systems is expected to be more challenging than for fcc (100) metal surfaces. It is recognized at least for island diffusion on these surfaces that concerted motion and possible formation of stacking-fault defects can play a role.[80−82] From the perspective of providing precise ab initio treatment of kinetics, our preliminary analysis indicates an additional challenge in that there is not a single TS geometry that applies for PD at different types of step edges. Thus, some refinement of the formulation developed in this Article, for example, to incorporate multiple TS, is required.

■ ASSOCIATED CONTENT

Ⓢ Supporting Information

The Supporting Information is available free of charge on the ACS Publications website at DOI: 10.1021/acs.jpcc.6b07328.

> General details of DFT analysis (section S1), results of PBE analysis (section S2), DFT analysis of step energies (section S3), and large-unit-cell determination of interactions for Ag(100) (section S4) (PDF)

■ AUTHOR INFORMATION

Corresponding Authors

*E-mail: yong@ameslab.gov.
*E-mail: evans@ameslab.gov.

Present Address

‖Department of Mechanical Engineering, University of Colorado, Boulder, Colorado 80309, United States.

Notes

The authors declare no competing financial interest.

■ ACKNOWLEDGMENTS

We thank Da-Jiang Liu for valuable discussions and insights into island coalescence processes. We also acknowledge the use of computational resources from NSF-supported XSEDE as well as USDOE-supported NERSC and OLCF. This work was supported by NSF grant CHE-1507223. It was performed at Ames Laboratory, which is operated for the U.S. Department of Energy by Iowa State University under contract no. DE-AC02-07CH11358.

■ REFERENCES

(1) Wen, J.-M.; Evans, J. W.; Bartelt, M. C.; Burnett, J. W.; Thiel, P. A. Coarsening Mechanisms in a Metal Film: From Cluster Diffusion to Vacancy Ripening. *Phys. Rev. Lett.* **1996**, *76*, 652−655.

(2) Stoldt, C. R.; Cadilhe, A. M.; Jenks, C. J.; Wen, J.-M.; Evans, J. W.; Thiel, P. A. Evolution of Far-From-Equilibrium Nanostructures Formed by Cluster-Step and Cluster-Cluster Coalescence in Metal Films. *Phys. Rev. Lett.* **1998**, *81*, 2950−2953.

(3) Morgenstern, K. Fast Scanning Tunnelling Microscopy as a Tool to Understand Changes on Metal Surfaces: from Nanostructures to Single Atoms. *Phys. Status Solidi B* **2005**, *242*, 773−796.

(4) Thiel, P. A.; Shen, M.; Liu, D.-J.; Evans, J. W. Coarsening of Two-Dimensional Nanoclusters on Metal Surfaces. *J. Phys. Chem. C* **2009**, *113*, 5047−5067.

(5) Jensen, P. Growth of Nanostructures by Cluster Deposition: Experiments and Simple Models. *Rev. Mod. Phys.* **1999**, *71*, 1695−1735.

(6) Datye, A. K.; Xu, Q.; Kharas, K. C.; McCarty, J. M. Particle Size Distributions in Heterogeneous Catalysts: What do They Tell Us about the Sintering Mechanism? *Catal. Today* **2006**, *111*, 59−67.

(7) Xia, Y.; Xiong, Y.; Lim, B.; Skrbalak, S. E. Shape-Controlled Synthesis of Metal Nanocrystals: Simple Chemistry Meets Complex Physics? *Angew. Chem., Int. Ed.* **2009**, *48*, 60−103.

(8) Privman, V. Colloids, Nanocrystals, and Surface Nanostructures of Uniform Size and Shape: Modeling of Nucleation and Growth in Solution Synthesis. In *Complex-Shaped Metal Nanoparticles: Bottom-Up Syntheses and Applications*; Sau, T. K., Rogach, A. L., Eds.; Wiley-VCH Verlag GmbH & Co. KGaA: Weinheim, Germany, 2012; Chapter 7, pp 239−268.

(9) Yuk, J. M.; Park, J.; Ercius, P.; Kim, K.; Hellebusch, D. J.; Crommie, M. F.; Lee, J. Y.; Zettl, A.; Alivisatos, A. P. High-Resolution EM of Colloidal Nanocrystal Growth Using Graphene Liquid Cells. *Science* **2012**, *336*, 61−64.

(10) Woehl, T. J.; Park, C.; Evans, J. E.; Arslan, I.; Ristenpart, W. D.; Browning, N. D. Direct Observation of Aggregative Nanoparticle Growth: Kinetic Modeling of the Size Distribution and Growth Rate. *Nano Lett.* **2014**, *14*, 373−378.

(11) Lim, T. H.; McCarthy, D.; Hendy, S. C.; Stevens, K. J.; Brown, S. A.; Tilley, R. D. Real-Time TEM and Kinetic Monte Carlo Studies of the Coalescence of Decahedral Gold Nanoparticles. *ACS Nano* **2009**, *3*, 3809−3813.

(12) Gorshkov, V.; Kuzmenko, V.; Privman, V. Nonequilibrium Kinetic Study of Sintering of Dispersed Nanoparticles. *CrystEngComm* **2013**, *15*, 7177−7191.

(13) Liu, D.-J.; Evans, J. W. Sintering of Two-Dimensional Nanoclusters in Metal (100) Homoepitaxial Systems: Deviations from Predictions of Mullins Continuum Theory. *Phys. Rev. B: Condens. Matter Mater. Phys.* **2002**, *66*, 165407.

(14) Jensen, P.; Combe, N.; Larralde, H.; Barrat, J. L.; Misbah, C.; Pimpinelli, A. Kinetics of Shape Equilibration for Two Dimensional Islands. *Eur. Phys. J. B* **1999**, *11*, 497−504.

(15) Combe, N.; Larralde, H. Low-Temperature Shape Relaxation of Two-Dimensional Islands by Edge Diffusion. *Phys. Rev. B: Condens. Matter Mater. Phys.* **2000**, *62*, 16074−16084.

(16) Pai, W. W.; Swan, A. K.; Zhang, Z.; Wendelken, J. F. Island Diffusion and Coarsening on Metal (100) Surfaces. *Phys. Rev. Lett.* **1997**, *79*, 3210−3213.

(17) Lagally, M. G.; Zhang, Z. Thin-film cliffhanger. *Nature* **2002**, *417*, 907−910.

(18) Kresse, G.; Furthmüller, J. Efficient Iterative Schemes for Ab Initio Total-Energy Calculations Using a Plane-Wave Basis Set. *Phys. Rev. B: Condens. Matter Mater. Phys.* **1996**, *54*, 11169−11186.

(19) Han, Y.; Liu, D.-J. Quantum Size Effects in Metal Nanofilms: Comparison of an Electron-Gas Model and Density Functional Theory Calculations. *Phys. Rev. B: Condens. Matter Mater. Phys.* **2009**, *80*, 155404.

(20) Han, Y.; Ünal, B.; Jing, D.; Thiel, P. A.; Evans, J. W.; Liu, D.-J. Nanoscale "Quantum" Islands on Metal Substrates: Microscopy Studies and Electronic Structure Analyses. *Materials* **2010**, *3*, 3965−3993.

(21) Perdew, J. P.; Ruzsinszky, A.; Csonka, G. I.; Vydrov, O. A.; Scuseria, G. E.; Constantin, L. A.; Zhou, X.; Burke, K. Restoring the Density-Gradient Expansion for Exchange in Solids and Surfaces. *Phys. Rev. Lett.* **2008**, *100*, 136406.

(22) Perdew, J. P.; Burke, K.; Ernzerhof, M. Generalized Gradient Approximation Made Simple. *Phys. Rev. Lett.* **1996**, *77*, 3865−3868.

(23) Pai, W. W.; Wendelken, J. F.; Stoldt, C. R.; Thiel, P. A.; Evans, J. W.; Liu, D.-J. Evolution of Two-Dimensional Wormlike Nanoclusters on Metal Surfaces. *Phys. Rev. Lett.* **2001**, *86*, 3088−3091.

(24) Einstein, T. L.; Sathiyanarayanan, R. Multisite Interactions in Lattice-Gas Models. In *Nanophenomena at Surfaces, Springer Series in Surface Sciences 47*; Michailov, M., Ed.; Springer-Verlag: Berlin, Heidelberg, 2011; Chapter 2, pp 19−37.

(25) Herder, L. M.; Bray, J. M.; Schneider, W. F. Comparison of Cluster Expansion Fitting Algorithms for Interactions at Surfaces. *Surf. Sci.* **2015**, *640*, 104−111.

(26) Sanchez, J. M. Cluster Expansion and the Configurational Theory of Alloys. *Phys. Rev. B: Condens. Matter Mater. Phys.* **2010**, *81*, 224202 and references therein..

(27) Sathiyanarayanan, R.; Stasevich, T. J.; Einstein, T. L. Sensitivity of Short-Range Trio Interactions to Lateral Relaxation of Adatoms: Challenges for Detailed Lattice-Gas Modeling. *Surf. Sci.* **2008**, *602*, 1243−1249.

(28) Evans, J. W.; Thiel, P. A.; Bartelt, M. C. Morphological Evolution during Epitaxial Thin Film Growth: Formation of 2D Islands and 3D Mounds. *Surf. Sci. Rep.* **2006**, *61*, 1−128.

(29) Brown, G.; Rikvold, P. A.; Mitchell, S. J.; Novotny, M. A. Monte Carlo Methods for Equilibrium and Nonequilibrium Problems in Interfacial Electrochemistry. In *Interfacial Electrochemistry: Theory, Experiment, and Application*; Wieckowski, A., Ed.; Marcel Dekker: New York, 1999; Chapter I.4, pp 47−61.

(30) Fichthorn, K. A.; Scheffler, M. Island Nucleation in Thin-Film Epitaxy: A First-Principles Investigation. *Phys. Rev. Lett.* **2000**, *84*, 5371−5374.

(31) Jansen, M. M. M.; Hermse, C. G. M.; Jansen, A. P. J. Kinetic Parameters from Temperature Programmed Desorption Spectra Combined with Energy Relations: Top and Bridge CO on Rh(100). *Phys. Chem. Chem. Phys.* **2010**, *12*, 8053−8061.

(32) Zhdanov, V. P. *Elementary Physicochemical Processes on Solid Surfaces*; Plenum: New York, 1991.

(33) Mehl, H.; Biham, O.; Furman, I.; Karimi, M. Models for Adatom Diffusion on fcc (001) Metal Surfaces. *Phys. Rev. B: Condens. Matter Mater. Phys.* **1999**, *60*, 2106−2116.

(34) Tiwary, Y.; Fichthorn, K. A. Mechanisms of Atomic Diffusion on the Flat, Stepped, and Faceted Surfaces of Al(110). *Phys. Rev. B: Condens. Matter Mater. Phys.* **2010**, *81*, 195421.

(35) Han, Y.; Jing, D.; Ünal, B.; Thiel, P. A.; Evans, J. W. Far-from-Equilibrium Film Growth on Alloy Surfaces: Ni and Al on NiAl(110). *Phys. Rev. B: Condens. Matter Mater. Phys.* **2011**, *84*, 113414.

(36) Han, Y.; Ünal, B.; Evans, J. W. Formation of a Novel Ordered Ni_3Al Surface Structure by Codeposition on NiAl(110). *Phys. Rev. Lett.* **2012**, *108*, 216102.

(37) Han, Y.; Liu, D.-J.; Evans, J. W. Real-Time Ab Initio KMC Simulation of the Self-Assembly and Sintering of Bimetallic Epitaxial Nanoclusters: Au + Ag on Ag(100). *Nano Lett.* **2014**, *14*, 4646−4652.

(38) Han, Y.; Evans, J. W. Directing Anisotropic Assembly of Metallic Nanoclusters by Exploiting Linear Trio Interactions and Quantum Size Effects: Au Chains on Ag(100) Thin Films. *J. Phys. Chem. Lett.* **2015**, *6*, 2194−2199.

(39) Liu, D.-J.; Stoldt, C. R.; Thiel, P. A.; Evans, J. W. Sintering of Metal(100) Homoepitaxial Islands: Kink Rounding Barriers, Modified Size Scaling, and Experimental Behavior. *MRS Online Proc. Libr.* **2003**, *749*, 35−40.

(40) Wendelken, J. F.; Swan, A. K.; Pai, W.-W.; Zuo, J.-K. Morphology and Energy Barriers in Homoepitaxial Growth and Coarsening: A Case Study for Cu(100). In *Morphological Organization in Epitaxial Growth and Removal*; Zhang, Z., Lagally, M.G., Eds.; Series on Directions in Condensed Matter Physics; World Scientific: Singapore, 1998; Vol. *14*, pp 320−348.

(41) Giesen, M. Step and Island Dynamics at Solid/Vacuum and Solid/Liquid Interfaces. *Prog. Surf. Sci.* **2001**, *68*, 1−153.

(42) Yu, B. D.; Scheffler, M. Ab Initio Study of Step Formation and Self-Diffusion on Ag(100). *Phys. Rev. B: Condens. Matter Mater. Phys.* **1997**, *55*, 13916−13924.

(43) Nelson, R. C.; Einstein, T. L.; Khare, S. V.; Rous, P. J. Energies of Steps, Kinks, and Defects on Ag{100} and Ag{111} Using the Embedded Atom Method, and Some Consequences. *Surf. Sci.* **1993**, *295*, 462−484.

(44) Stasevich, T. J.; Einstein, T. L.; Zia, R. K. P.; Giesen, M.; Ibach, H.; Salzma, F. Effects of Next-Nearest-Neighbor Interactions on the Orientation Dependence of Step Stiffness: Reconciling Theory with Experiment for Cu(001). *Phys. Rev. B: Condens. Matter Mater. Phys.* **2004**, *70*, 245404.

(45) Kellogg, G. L. Field ion microscope studies of single-atom surface diffusion and cluster nucleation on metal surfaces. *Surf. Sci. Rep.* **1994**, *21*, 1−88.

(46) Cadilhe, A. M.; Stoldt, C. R.; Jenks, C. J.; Thiel, P. A.; Evans, J. W. Evolution of Far-from-Equilibrium Nanostructures on Ag(100) Surfaces: Protrusions and Indentations at Extended Step Edges. *Phys. Rev. B: Condens. Matter Mater. Phys.* **2000**, *61*, 4910−4925.

(47) Henkelman, G.; Jónsson, H. Improved Tangent Estimate in the Nudged Elastic Band Method for Finding Minimum Energy Paths and Saddle Points. *J. Chem. Phys.* **2000**, *113*, 9978−9985.

(48) Khare, S. V.; Bartelt, N. C.; Einstein, T. L. Diffusion of Monolayer Adatom and Vacancy Clusters: Langevin Analysis and Monte Carlo Simulations of their Brownian Motion. *Phys. Rev. Lett.* **1995**, *75*, 2148−2151.

(49) Krug, J.; Dobbs, H. T.; Majaniemi, S. Adatom Mobility for the Solid-on-Solid Model. *Z. Phys. B: Condens. Matter* **1995**, *97*, 281−291.

(50) Stasevich, T. J.; Einstein, T. L.; Stolbov, S. Extended Lattice Gas Interactions of Cu on Cu(111) and Cu(001): Ab Initio Evaluation and Implications. *Phys. Rev. B: Condens. Matter Mater. Phys.* **2006**, *73*, 115426.

(51) Li, W.; Huang, L.; Evans, J. W.; Han, Y. Submonolayer Ag Films on Fe(100): A First-Principles Analysis of Energetics Controlling Adlayer Thermodynamics and Kinetics. *Phys. Rev. B: Condens. Matter Mater. Phys.* **2016**, *93*, 155416.

(52) Giesen, M.; Steimer, C.; Ibach, H. What does One Learn from Equilibrium Shapes of Two-Dimensional Islands on Surfaces? *Surf. Sci.* **2001**, *471*, 80−100.

(53) Dieluweit, S.; Ibach, H.; Giesen, M.; Einstein, T. L. Orientation Dependence of the Cu(001) Surface Step Stiffness: Failure of Solid-on-Solid and Ising Models to Describe Experimental Data. *Phys. Rev. B: Condens. Matter Mater. Phys.* **2003**, *67*, 121410.

(54) Moere, R. V.; Zandvliet, H. J. W.; Poelsema, B. Two-Dimensional Equilibrium Island Shape and Step Free Energies of Cu(001). *Phys. Rev. B: Condens. Matter Mater. Phys.* **2003**, *67*, 193407.

(55) H. J. W; Poelsema, M. R. V.; Zandvliet, B. Free Energy and Stiffness of ⟨110⟩ and ⟨010⟩ Steps on a ⟨001⟩ Surface of a Cubic Lattice: Revival of the Solid-on-Solid Model. *Phys. Rev. B: Condens. Matter Mater. Phys.* **2003**, *68*, 073404.

(56) Tiwary, Y.; Fichthorn, K. A. Connector Model for Describing Many-Body Interactions at Surfaces. *Phys. Rev. B: Condens. Matter Mater. Phys.* **2008**, *78*, 205418.

(57) Zandvliet, H. Energetics of Si(001). *Rev. Mod. Phys.* **2000**, *72*, 593−602.

(58) Tung, R. T.; Graham, W. R. Single Atom Self-diffusion on Nickel Surfaces. *Surf. Sci.* **1980**, *97*, 73−87.

(59) Chang, C. M.; Wei, C. M.; Hafner, J. Self-Diffusion of Adatoms on Ni(100) Surfaces. *J. Phys.: Condens. Matter* **2001**, *13*, L321−L328.

(60) Feibelman, P. J. Scaling of Hopping Self-Diffusion Barriers on fcc(100) Surfaces with Bulk Bond Energies. *Surf. Sci.* **1999**, *423*, 169−174.

(61) Ayrault, G.; Ehrlich, G. Surface Self-Diffusion on an fcc Crystal: An Atomic View. *J. Chem. Phys.* **1974**, *60*, 281−294.

(62) Evans, J. W.; Flynn-Sanders, D. K.; Thiel, P. A. Surface Self-Diffusion Barrier of Pd(100) from Low-Energy Electron Diffraction. *Surf. Sci.* **1993**, *298*, 378−383.

(63) Feibelman, P. J.; Stumpf, R. Adsorption-Induced Lattice Relaxation and Diffusion by Concerted Substitution. *Phys. Rev. B: Condens. Matter Mater. Phys.* **1999**, *59*, 5892−5897.

(64) Chang, C. M.; Wei, C. M. Self-diffusion of Adatoms and Dimers on fcc(100) Surfaces. *Chin. J. Phys.* **2005**, *43*, 169−175.

(65) Kopatzki, E.; Günther, S.; Nichtl-Pecher, W.; Behm, R. J. Homoepitaxial Growth on Ni(100) and Its Modification by a Preadsorbed Oxygen Adlayer. *Surf. Sci.* **1993**, *284*, 154−166.

(66) Hoogenman, M. S.; Klik, M. A.; van Gastel, R.; Frenken, J. W. M. On the Smoothing of Rough Surfaces. *J. Phys.: Condens. Matter* **1999**, *11*, 4349−4365.

(67) Stroscio, J. A.; Pierce, D. T.; Dragoset, R. A. Homoepitaxial Growth of Iron and a Real Space View of Reflection-High-Energy-Electron Diffraction. *Phys. Rev. Lett.* **1993**, *70*, 3615−3618.

(68) Hsieh, T. C.; Shapiro, A. P.; Chiang, T.-C. Core-level Shifts for Au Epitaxial Overlayers on Ag. *Phys. Rev. B: Condens. Matter Mater. Phys.* **1985**, *31*, 2541−2544.

(69) Paggel, J. J.; Miller, T.; Chiang, T.-C. Quantum-Well States as Fabry-Pérot Modes in a Thin-Film Electron Interferometer. *Science* **1999**, *283*, 1709−1711.

(70) Man, K. L.; Qiu, Z. Q.; Altman, M. S. Kinetic Limitations in Electronic Growth of Ag Films on Fe(100). *Phys. Rev. Lett.* **2004**, *93*, 236104.

(71) Evans, J. W.; Flynn, D. K.; Thiel, P. A. Influence of Adsorption-Site Geometry and Diffusion on Thin-Film Growth: Pt/Pd(100). *Ultramicroscopy* **1989**, *31*, 80−86.

(72) Beauvais, S. L.; Behm, R. J.; Chang, S.-L.; King, T. S.; Olson, C. G.; Rape, P. R.; Thiel, P. A. Reconstruction in a Thin Film: Epitaxial Pt on Pd(100). *Surf. Sci.* **1987**, *189−190*, 1069−1075.

(73) Zhang, L.; Roling, L. T.; Wang, X.; Vara, M.; Chi, M.; Liu, J.; Chou, S.-I.; Park, J.; Herron, J. A.; Xie, Z.; Mavrikakis, M.; Xia, Y. Platinum-Based Nanocages with Subnanometer-Thick Walls and Well-Defined, Controllable Facets. *Science* **2015**, *349*, 412−416.

(74) Jette, E. R.; Foote, F. Precision Determination of Lattice Constants. *J. Chem. Phys.* **1935**, *3*, 605−616.

(75) Eßer, M.; Morgenstern, K.; Rosenfeld, G.; Comsa, C. Dynamics of vacancy island coalescence on Ag(111). *Surf. Sci.* **1998**, *402−404*, 341−345.

(76) Hamouda, A. B.; Sathiyanarayanan, R.; Pimpinelli, A.; Einstein, T. L. Role of Codeposited Impurities during Growth. I. Explaining Distinctive Experimental Morphology on Cu(001). *Phys. Rev. B: Condens. Matter Mater. Phys.* **2011**, *83*, 035423.

(77) Ling, W. L.; Bartelt, N. C.; Pohl, K.; de la Figuera, J.; Hwang, R. Q.; McCarty, K. F. Enhanced Self-Diffusion on Cu(111) by Trace Amounts of S: Chemical-Reaction-Limited Kinetics. *Phys. Rev. Lett.* **2004**, *93*, 166101.

(78) Walen, H.; Liu, D.-J.; Oh, J.; Lim, H.; Evans, J. W.; Aikens, C. M.; Kim, Y.; Thiel, P. A. Cu_2S_3 Complex on Cu(111) as a Candidate for Mass Transport Enhancement. *Phys. Rev. B: Condens. Matter Mater. Phys.* **2015**, *91*, 045426.

(79) Rosenfeld, G.; Morgenstern, K.; Esser, M.; Comsa, G. Dynamics and Stability of Nanostructures on Metal Surfaces. *Appl. Phys. A: Mater. Sci. Process.* **1999**, *69*, 489−496.

(80) Hamilton, J. C. Magic Size Effects for Heteroepitaxial Island Diffusion. *Phys. Rev. Lett.* **1996**, *77*, 885−888.

(81) Karim, A.; Kara, A.; Trushin, O.; Rahman, T. S. The Crossover from Collective Motion to Periphery Diffusion for Two-Dimensional Adatom-Islands on Cu(111). *J. Phys.: Condens. Matter* **2011**, *23*, 462201.

(82) Shah, S. I.; Nandipati, G.; Karim, A.; Rahman, T. S. Self-Learning Kinetic Monte Carlo Simulations of Self-Diffusion of Small Ag Islands on the Ag(111) Surface. *J. Phys.: Condens. Matter* **2016**, *28*, 025001.

Supporting Information

for **“Ab Initio Thermodynamics and Kinetics for Coalescence of Two-Dimensional Nanoislands and Nanopits on Metal (100) Surfaces”**

Yong Han,[1*] Conrad R. Stoldt,[2] Patricia A. Thiel,[2,3] and James W. Evans[1,3*]

[1]Department of Physics and Astronomy, Iowa State University, Ames, Iowa 50011, United States

[2]Department of Chemistry, Iowa State University, Ames, Iowa 50011, United States

[3]Ames Laboratory - U. S. DOE, Iowa State University, Ames, Iowa 50011, United States

S1. General Details of DFT Analysis

In our DFT total-energy calculations, we use the periodically-repeated slabs to represent the surface.[1] The vacuum thickness between adjacent slabs is never less than 1.5 nm to avoid interaction between slabs. The projector augmented-wave (PAW) method[2] is utilized for the electron-core interactions with the pseudopotentials released in 2013 by the VASP group. The energy cutoffs of the plane-wave basis for metals other than Ag are set to be VASP default values, which suffices for accurate assessment of energetics discussed in this work. For the Ag system on which we focus, a larger energy cutoff of 400 eV versus the VASP default value of 249.844 eV is utilized.

To avoid corruption of our determination of surface energetics for (100) surfaces of single-crystal substrates due to QSE-induced oscillations of electronic properties with varying thickness of thin slabs,[3,4] we choose a thick-enough slab up to 15 MLs. We note that QSE are particularly strong for Ag and Cu. However, when only rough estimates are needed for some energies, we just use a 4- or 5-ML slab, as was actually selected in most of previous literature. Γ-centered $\boldsymbol{k}$ meshes are carefully tested for any lateral sizes of supercells, e.g., we choose 31×31 $\boldsymbol{k}$ mesh for 1×1 unit cell, 9×9 $\boldsymbol{k}$ mesh for 4×4 unit cell, 7×9 $\boldsymbol{k}$ mesh for 5×4 unit cell, etc.

During energy minimization, the bottommost 8 MLs are fixed for a 15-ML slab (as is the bottommost 1 ML is fixed for a 4- or 5-ML slab) and other atoms are allowed to relax until the self-consistent forces reach the tolerance of 0.1 eV/nm. Before energy minimization, all atoms in the slab are at their corresponding bulk-crystal positions with the DFT lattice constants for bulk: $a_{\mathrm{Ag}} = 0.4147$ (0.4053) nm from PBE (PBEsol), $a_{\mathrm{Cu}} = 0.3634$ (0.3569) nm from PBE (PBEsol), $a_{\mathrm{Pd}} = 0.3940$ (0.3872) nm from PBE (PBEsol), $a_{\mathrm{Ni}} = 0.3517$ nm from PBE, $a_{\mathrm{Rh}} = 0.3824$ nm from PBE, $a_{\mathrm{Nb}} = 0.3321$ nm from PBE, and $a_{\mathrm{Ta}} = 0.3321$ nm from PBE. All these DFT values of lattice constants that we obtained are in good agreement with experimental values.[5]

The key quantity extracted in our DFT analysis is the adlayer energy per adatom, E_ν, where ν represents corresponding configuration containing M adlayer atoms per unit cell. This adlayer energy equals the sum of the total adsorption plus the total lateral interaction energy within the unit cell divided by M. It is obtained from

$$E_{\nu} = E_{\mathrm{tot}} - E_{\mathrm{slab}} - ME_{\mathrm{o}}, \tag{S1}$$

where E_{tot} is the total energy of the slab plus adlayer atoms, E_{slab} is the energy of the slab without adlayer atoms, and E_{o} is the self-energy of one isolated gas-phase atom. E_{tot}, E_{slab}, and E_{o} are directly obtained from DFT calculations.

S2. Results of PBE Analysis

We also have used the PBE functional to repeat the majority of the DFT analysis which was reported in the main text based on the PBEsol functional. We start by reviewing results for Ag and Cu. *First*, we assess E_{ν} for the same key configurations ν as considered in Table 1. Corresponding PBE values for these E_{ν} are given in Table S1. The PBE value of E_{4fh} for isolated atoms identified as $E_{\mathrm{p}(4\times4)}$ is ~83% (87%) of the PBEsol value for Ag (Cu). The PBE value of the "true" $\omega_{\mathrm{p1}} \approx 2\left[E_{(4\times4)\text{-NN}} - E_{\mathrm{4fh}}\right] = -0.234\ (-0.332)$ eV for Ag (Cu) is 80% (87%) of the PBEsol value. The effective $\omega_{\mathrm{p1}}^{\mathrm{eff}} = \left[E_{\mathrm{p}(1\times1)} - E_{\mathrm{4fh}}\right]/2 = -0.206\ (-0.298)$ eV for Ag (Cu) is 77% (84%) of PBEsol value. *Second*, we consider quantities related to step-edge thermodynamics noting that PBE values for $E_{\mathrm{e}}^{\mathrm{form}}$ and $\Delta E_{\langle 110\rangle}$ are ~80% (~87%) below PBEsol values for Ag (Cu); see Table S2. *Third*, we consider diffusion barriers for terrace and step-edge diffusion. PBE values are generally ~82% (~88%) below PBEsol values for Ag (Cu); see Table S3. Thus, a consistent discrepancy between PBE and PBEsol values for this diverse collection of energies is apparent, the former generally being ~78–84% (84–88%) of the latter.

Table S1. E_{ν} (in eV) from PBE for Ag(100) and Cu(100).

	$E_{\mathrm{p}(4\times4)}$	$E_{(4\times4)\text{-NN}}$	$E_{\mathrm{c}(2\times2)}$	$E_{\mathrm{p}(1\times1)}$
Ag	–2.106	–2.222	–2.143	–2.517
Cu	–2.886	–3.052	–2.965	–3.482

Table S2. Thermodynamic Energies (in eV) from PBE for Straight Steps of Ag(100) and Cu(100).

	$E_{\mathrm{e}}^{\mathrm{form}}$	$\Delta E_{\langle 110\rangle}$	$\Delta E_{\langle 100\rangle}$
Ag	0.192	0.377	0.010
Cu	0.262	0.519	0.023

We compare our PBE results against selected previous analyses. A PBE analysis by Liu[6] used a 4 × 4 unit cell, averaged over slabs of 8–15 MLs to avoid QSEs, to obtain the ω_{p1} = 0.22 (0.32) eV and $E_{\mathrm{d}} = 0.440\ (0.542)$ eV for Ag (Cu), consistent with our analysis. Another study[7] used the PW91 functional but just 5-ML slabs (where results are influenced by

QSEs) to obtain $E_{\mathrm{d}} = 0.45$ (0.53) eV for hopping, $E_{\mathrm{d}} = 0.59$ (0.79) eV for exchange, and $E_{\mathrm{e}} = 0.24$ (0.32) eV for edge diffusion for Ag (Cu). All these values are quite close to our PBE results. Finally, we note that PW91 values[8] for conventional interactions obtained by a conventional CE approach of $\omega_{\mathrm{p1}} = -0.335$, $\omega_{\mathrm{p2}} = -0.043$, $\omega_{\mathrm{t1}} = +0.054$, $\omega_{\mathrm{t2}} = -0.016$ also appear consistent with our PBE energetics for Cu.

Table S3. Activation Barriers (in eV) for Hopping on Key Step-Edge Diffusion Processes form PBE for Ag(100) and Cu(100).[a]

	E_{e}	E_{kr}	E_{s}
Ag	0.234	0.427	0.483
Cu	0.295	0.551	0.597

[a]We also obtain $E_{\mathrm{d}} = 0.447$ (0.548) eV for Ag (Cu).

Numerous DFT analyses of energetics for these and other systems generally do not provide a detailed assessment of the extent to which those values are compatible with experimental observations. We have a considerable advantage for Ag(100) since extensive data on both island formation and post-deposition relaxation is available. From the analysis in Section 6, it is clear that the PBE prediction for $E_{\mathrm{eff}} = E_{\mathrm{e}}^{\mathrm{form}} + E_{\mathrm{e}} + E_{\mathrm{kr}}$ and its constituent energies is too small in magnitude and predict coalescence times well below experimental observations. In contrast, PBEsol values reasonably recover observed behavior. It should however be noted that PBEsol values for terrace-diffusion barriers appear too high to recover observed island densities formed during deposition. Significant dimer diffusion in the nucleation process[9] would allow experimental densities to be matched by higher E_{d}, but still below the PBEsol value.[10] Also Arrhenius behavior of the island density appears more consistent with lower PBE values of E_{d}.[9]

Finally, while it is well-accepted that the hopping pathway dominates exchange for terrace diffusion for Ag(100) and Cu(100) homoepitaxy, there is less consideration of the possibility that exchange rather than hopping might dominate kink rounding. Consequently, we have utilized the cNEB approach to assess the two-atom near-kink exchange barrier for the pathway shown in Figure 2g, using a 4-ML slab of 5 × 5 unit cell for Cu(100) homoepitaxy. The obtained PBE exchange barrier is 0.705 eV compared to a hopping barrier of 0.577 eV for the direct corner rounding of only one adatom. Thus, the direct hopping is favored over the two-atom near-kink exchange for kink rounding. We expect that the same behavior would be found for Ag(100). While we have not performed DFT cNEB analysis for this case, we have checked that analysis by using interactions from the embedded-atom method (EAM), predicting that hopping is favored over exchange for Ag(100) surface.

Here we also provide our PBE results of key barriers for Pd/Pd(100); see Table S4. We also determine $E_{\mathrm{4fh}} \approx E_{\mathrm{p(4\times4)}} = -3.213$ eV, $E_{\mathrm{p(4\times4)\text{-}NN}} = -3.327$ eV, and $E_{\mathrm{p(1\times1)}} = -3.743$

eV, so that the “true” $\omega_{\mathrm{p1}} = 2\left[E_{\mathrm{p(4\times4)\text{-}NN}} - E_{\mathrm{4fh}}\right] = -0.228$ eV and $\omega_{\mathrm{p1}}^{\mathrm{eff}} = \left[E_{\mathrm{p(1\times1)}} - E_{\mathrm{4fh}}\right]/2 = -0.265$ eV from PBE analyses. For more details of calculations, see Section S1.

Table S4. DFT PBE Estimates of Activation Barriers (in eV) for Key Diffusion Processes for Pd/Pd(100).

E_{d} (hop)	E_{d} (exchange)	E_{e}	δ_{kr}	E_{kr}
0.818	0.887	0.449	0.370	0.819

S3. DFT Analysis of Step Energies

In Section 2, we have described the determination of step energies by analyzing the total energy for a slab with periodically-alternating ascending-and-descending steps of a specified orientation.[11] Subtraction of surface- and bulk-energy components can lead to significant errors. For this reason, we adopt here a different strategy comparing suitably-selected pairs of configurations to enable direct cancellation of bulk and surface contributions.

Of particular interest is determination of some measure of the difference between step energies for ⟨110⟩ and ⟨100⟩ orientations. To this end, we compare the total energies for configurations with a 1/2 ML strip on a 15-ML slab. For step edges along the ⟨110⟩ direction we use a 12 × 1 unit cell, and for step edges along the ⟨100⟩ direction we use a $6\sqrt{2} \times \sqrt{2}$ unit cell, so both analyses involve the same total number of atoms and the same number of surface atoms. Accounting for the feature that each configuration involves two steps, the energy difference equals $2\left(\sqrt{2}a\beta_{\langle 100\rangle} - a\beta_{\langle 110\rangle}\right)$. From such an analysis, we obtain PBE values of $\sqrt{2}a\beta_{\langle 100\rangle} - a\beta_{\langle 110\rangle} = 0.096\ (0.129)$ eV for Ag (Cu). Similarly, we obtain PBEsol values of $\sqrt{2}a\beta_{\langle 100\rangle} - a\beta_{\langle 110\rangle} = 0.118\ (0.157)$ eV for Ag (Cu). We note that from Equations 4–6, it immediately follows that

$$4\left(\sqrt{2}a\beta_{\langle 100\rangle} - a\beta_{\langle 110\rangle}\right) = \Delta E_{\langle 110\rangle} - \omega_{\mathrm{t2}} - \cdots \approx \Delta E_{\langle 110\rangle}. \qquad \text{(S2)}$$

Compared with $\Delta E_{\langle 110\rangle}$ values in Tables 1 and S2, our DFT results from quite different types of analyses are reasonably consistent with the relationship Equation S2.

In addition, we have performed a direct analysis of $a\beta_{\langle 110\rangle}$ by comparing the energy of two configurations both based on a 16 × 1 unit cell. The first has a strip of width $8a$ and the second has two strips of width $4a$ (each separated by 4 empty rows). The difference in the total energy of these two configurations equals $2a\beta_{\langle 110\rangle}$. For this analysis we obtain PBE estimates of $a\beta_{\langle 110\rangle} = 0.100\ (0.148)$ eV for Ag (Cu). PBEsol analysis yields $a\beta_{\langle 110\rangle} = 0.131\ (0.178)$ eV for Ag (Cu).

For comparison, we note that early LDA analysis[11] based on the approach described in Section 2 and for very small systems yielded estimates of $a\beta_{\langle 110\rangle} = 0.130$ eV and $a\beta_{\langle 100\rangle} = 0.156$ eV for Ag(100). Note that experimental results are available for Cu(100) for $a\beta_{\langle 110\rangle} = 0.22$ and $a\beta_{\langle 100\rangle} = 0.27$,[12] so that $\sqrt{2}a\beta_{\langle 100\rangle} - a\beta_{\langle 110\rangle} = 0.162$ eV very close to our PBEsol value of 0.157 eV (although the PBEsol estimate of $a\beta_{\langle 110\rangle}$ is somewhat below the experimental value).

S4. Large-Unit-Cell Determination of Interactions for Ag(100)

Large-unit-cell calculations are expensive. Here, we present a limited analysis using a 6×6 unit cell but a thin 4-ML Ag(100) slab (and thus not eliminating QSEs which significantly modify at least weaker interactions).[6] However, the results (in eV) still provide an estimate of what we have described as "true" interactions: $E_{\mathrm{4fh}} = -2.118$, $E_{\mathrm{d}} = 0.430$, $\omega_{\mathrm{p1}} = -0.203$, $\omega_{\mathrm{p2}} = -0.003$, $\omega_{\mathrm{t1}} = +0.040$, $\omega_{\mathrm{t2}} = -0.044$. $\phi_{\mathrm{p1}} = -0.213$, $\phi_{\mathrm{t1}} = +0.110$, $\phi_{\mathrm{t2}} = -0.005$, $\phi_{\mathrm{t3}} = -0.032$, $\phi_{\mathrm{t4}} = +0.047$, $\phi_{\mathrm{t5}} = +0.011$. Note that this analysis used the pre-2013 version of PAW PBE GGA functional.

REFERENCES

(1) Kresse, G.; Furthmüller, J. Efficient Iterative Schemes for Ab Initio Total-Energy Calculations Using a Plane-Wave Basis Set. Phys. Rev. B 1996, 54, 11169–11186.

(2) Kresse, G.; Joubert, D. From Ultrasoft Pseudopotentials to the Projector Augmented-Wave Method. *Phys. Rev. B* **1999**, *59*, 1758–1775.

(3) Han, Y.; Liu, D.-J. Quantum Size Effects in Metal Nanofilms: Comparison of an Electron-Gas Model and Density Functional Theory Calculations. *Phys. Rev. B* **2009**, *80*, 155404.

(4) Han, Y.; Ünal, B.; Jing, D.; Thiel, P. A.; Evans, J. W.; Liu, D.-J. Nanoscale "Quantum" Islands on Metal Substrates: Microscopy Studies and Electronic Structure Analyses. *Materials* **2010**, *3*, 3965–3993.

(5) Kittel, C. *Introduction to Solid State Physics*, 7thed. John Wiley & Sons, Inc., New York, **1996**.

(6) Liu, D.-J. Density Functional Analysis of Key Energetics in Metal Homoepitaxy: Quantum Size Effects in Periodic Slab Calculations. *Phys. Rev. B* **2010**, *81*, 035415.

(7) Yildirim H.; Rahman, T. S. Diffusion Barriers for Ag and Cu Adatoms on the Terraces and Step Edges on Cu(100) and Ag(100): An Ab Initio Study. *Phys. Rev. B* **2009**, *80*, 235413.

(8) Stasevich, T. J.; Einstein, T. L.; Stolbov, S. Extended Lattice Gas Interactions of Cu on Cu(111) and Cu(001): Ab Initio Evaluation and Implications. *Phys. Rev. B* **2006**, *73*, 115426.

(9) Evans, J. W.; Thiel, P. A.; Bartelt, M. C. Morphological Evolution during Epitaxial Thin Film Growth: Formation of 2D Islands and 3D Mounds, *Surf. Sci. Rep.* **2006**, *61*, 1–128.

(10) Han, Y.; Liu, D.-J.; Evans, J. W. Real-Time Ab Initio KMC Simulation of the Self-Assembly and Sintering of Bimetallic Epitaxial Nanoclusters: Au + Ag on Ag(100). *Nano Lett.* **2014**, *14*, 4646–4652.

(11) Yu B. D.; Scheffler, M. Ab Initio Study of Step Formation and Self-Diffusion on Ag(100). *Phys. Rev. B* **1997**, *55*, 13916–13924.

(12) Giesen, M. Step and Island Dynamics at Solid/Vacuum and Solid/Liquid Interfaces. *Prog. Surf. Sci.* **2001**, *68*, 1–153.